HOKKAIDO UNIVERSITY

Title	Effect of degree of substitution on the microphase separation and mechanical properties of cellooligosaccharide acetate-based elastomers
Author(s)	Katsuhara, Satoshi; Sunagawa, Naoki; Igarashi, Kiyohiko et al.
Citation	Carbohydrate Polymers, 316, 120976 https://doi.org/10.1016/j.carbpol.2023.120976
Issue Date	2023-09-15
Doc URL	https://hdl.handle.net/2115/92207
Rights	© <2023>. This manuscript version is made available under the CC-BY-NC-ND 4.0 license http://creativecommons.org/licenses/by-nc-nd/4.0/
Rights(URL)	https://creativecommons.org/licenses/by-nc-nd/4.0/
Type	journal article
File Information	Carbohydrate Polymers 316 120976 .pdf

Hokkaido University Collection of Scholarly and Academic Papers : HUSCAP

Effect of degree of substitution on the microphase separation and mechanical properties of cellooligosaccharide acetate-based elastomers

Satoshi Katsuhara,[a] Naoki Sunagawa,[b] Kiyohiko Igarashi,[b,c] Yutaka Takeuchi,[d] Kenji Takahashi,[e] Takuya Yamamoto,[f] Feng Li,[f] Kenji Tajima, *[,f] Takuya Isono, *[,f] Toshifumi Satoh*[,f]

[a]*Graduate School of Chemical Sciences and Engineering, Hokkaido University, Sapporo 060-8628, Japan*

[b]*Department of Biomaterial Sciences, Graduate School of Agriculture and Life Sciences, The University of Tokyo, Tokyo 113-8657, Japan*

[c]*VTT Technical Research Centre of Finland Ltd., VTT FI-02044, Finland*

[d]*Noto Center for Fisheries Science and Technology, Faculty of Biological Science and Technology, Kanazawa University, Noto-cho, Ishikawa 927-0552, Japan*

[e]*Faculty of Biological Science and Technology, Institute of Science and Engineering, Kanazawa University, Kanazawa 920-1192, Japan*

[f]*Faculty of Engineering, Hokkaido University, Sapporo 060-8628, Japan*

Corresponding Authors

Kenji Tajima – *Faculty of Engineering, Hokkaido University, Sapporo 060-8628, Japan;* ORCID 0000-0003-3764-2084; Email: ktajima@eng.hokudai.ac.jp; Phone number: +81-11-706-6567

Takuya Isono – *Faculty of Engineering, Hokkaido University, Sapporo 060-8628, Japan;* ORCID 0000-0003-3746-2084; Email: isono.t@eng.hokudai.ac.jp; Phone number: +81-11-706-2290

Toshifumi Satoh – *Faculty of Engineering, Hokkaido University, Sapporo 060-8628, Japan;* ORCID 0000-0001-5449-9642; Email: satoh@eng.hokudai.ac.jp; Phone number: +81-11-706-6602

Abstract

Thermoplastic elastomers (TPEs) have long been used in a wide range of industries. However, most existing TPEs are petroleum-derived polymers. To realize environmentally benign alternatives to conventional TPEs, cellulose acetate is a promising TPE hard segment because of its sufficient mechanical properties, availability from renewable sources, and biodegradability in natural environments. Because the degree of substitution (DS) of cellulose acetate governs a range of physical properties, it is a useful parameter for designing novel cellulose acetate-based TPEs. In this study, we synthesized cellulose acetate-based ABA-type triblock copolymers ($AcCel_x$-*b*-PDL-*b*-$AcCel_x$) containing a celloologosaccharide acetate hard A segment ($AcCel_x$, where x is the DS; x = 3.0, 2.6, and 2.3) and a poly(*δ*-decanolactone) (PDL) soft B segment. Small-angle X-ray scattering showed that decreasing the DS of $AcCel_x$-*b*-PDL-*b*-$AcCel_x$ resulted in the formation of a more ordered microphase-separated structure. Owing to the microphase separation of the hard cellulosic and soft PDL segments, all the $AcCel_x$-*b*-PDL-*b*-$AcCel_x$ samples exhibited elastomer-like properties. Moreover, the decrease in DS improved toughness and suppressed stress relaxation. Furthermore, preliminary biodegradation tests in an aqueous environment revealed that the decrease in DS endowed $AcCel_x$-*b*-PDL-*b*-$AcCel_x$ with greater biodegradability potential. This work demonstrates the usefulness of cellulose acetate-based TPEs as next-generation sustainable materials.

Keywords: thermoplastic elastomer, cellulose acetate, mechanical properties, biodegradability, microphase separation, self-assembly

1. Introduction

Thermoplastic elastomers (TPEs) are essential materials in daily life and have been used in various fields. The hot-melt processability and reusability of TPEs are major advantages over conventional vulcanized rubbers, the thermoset nature of which prevents recycling. Most TPEs are ABA-type triblock copolymers, where the A block is an amorphous or semicrystalline polymer with a high glass transition temperature (T_g) and the B block is an amorphous rubbery polymer with a low T_g. Microphase separation into the "hard" A domain and the "soft" B matrix plays a key role in the elastic properties, with the hard A segments serving as physical crosslinks for the rubbery B chains. Commonly, TPEs utilize polystyrene (PS) as the hard segment, and various PS-based TPEs have been commercialized, as exemplified by PS-*b*-polyisoprene-*b*-PS, PS-*b*-polybutadiene-*b*-PS, and PS-*b*-polyethylenepropylene-*b*-PS (Maji & Naskar, 2022). However, these TPEs are derived from petroleum and lack biodegradability. Considering the recent demand for bio-based and biodegradable plastics, it is necessary to develop new environmentally benign TPEs. Various research groups have investigated bio-based and biodegradable alternatives to PS-based TPEs. For

---

Abbreviations: thermoplastic elastomer (TPE), glass transition temperature (T_g), polystyrene (PS), polylactide (PLA), block copolymer (BCP), poly(δ-decalactone) (PDL), degree of substitution (DS), tetrahydrofuran (THF), cellulose acetate ($AcCel_x$), small-angle X-ray scattering (SAXS), atomic force microscopy (AFM), propargyl-functionalized cellooligosaccharide (Cel–C≡CH), cellodextrin phosphorylase (CDP), α-D-glucose-1-phosphate (αG1P), dispersity ($Đ$), degree of polymerization (DP), matrix-assisted laser desorption/ionization time-of-flight mass spectrometry (MALDI-TOF MS), size-exclusion chromatography (SEC), differential scanning calorimetry (DSC), thermogravimetric analysis (TGA), wide-angle X-ray diffraction (WAXD), body-centered cubic (BCC), fast Fourier transform (FFT), order–disorder temperature (T_{ODT}), full width at half maximum (FWHM), Flory–Huggins interaction parameter (χ), Young's modulus (E), strain at break (ε_b), stress at break (σ_b), hexagonal cylinder (HEX), scanning electron microscopy (SEM)

instance, TPEs with polylactide (PLA) hard segments combined with amorphous and low-T_g aliphatic polyesters such as poly(β-methyl-δ-valerolactone), poly(ε-decalactone), and poly(menthide) as soft segments have been fabricated (Fournier, Riversa, & Hillmyer, 2022; Liffland & Hillmyer, 2021; Martello, Schneiderman, & Hillmyer, 2014; Shin et al., 2011; Watts & Hillmyer, 2019; Watts, Kurokawa, & Hillmyer, 2017).

Most bio-based TPEs utilize PLA as the hard segment, but poly-/oligosaccharides have potential as novel biodegradable hard segments. From a physiochemical point of view, oligosaccharides are highly attractive hard domains because of their reasonable solubility, high T_g (>100 °C), rigidity, and strong intermolecular interactions via hydrogen bonding or crystallization. Advantageously, oligosaccharides are also strongly incompatible with hydrophobic polymers, which leads to the formation of microphase-separated structures. Our previous study revealed that block copolymers (BCPs) consisting of maltooligosaccharide with a wide variety of hydrophobic polymers such as PS, poly(ε-caprolactone), poly(propylene oxide), polydimethylsiloxane, and oligoisoprene self-assembled into highly ordered microphase-separated structures with domain spacings (d) of less than 10 nm (Isono et al., 2013, 2019, 2022; Isono, Komaki, et al., 2020; Katsuhara et al., 2020; Mumtaz et al., 2020; Nishimura et al., 2022). These oligosaccharide-based BCPs formed microphase-separated structures easily, which indicates an unusually high potential for microphase separation. In addition, we have revealed that fully bio-based ABA-type triblock copolymers containing maltooligosaccharide as the A block and bio-based poly(δ-decalactone) (PDL; $T_g \approx -60$ °C) as the B block had highly ordered microphase-separated structures and exhibited elastomeric properties, with a stress at break of ~700% and a Young's modulus comparable to that of conventional PS-based TPEs (Isono, Nakahira, et al., 2020). Recently, we replaced unprotected maltooligosaccharide with cellulose triacetate to endow the BCPs with enhanced thermoplasticity. Compared with their amylose triacetate-based counterparts, the cellulose triacetate-based TPEs exhibited a greater self-assembly tendency and superior mechanical performance, likely due to stronger intermolecular interactions (Katsuhara et al., 2021). Because of

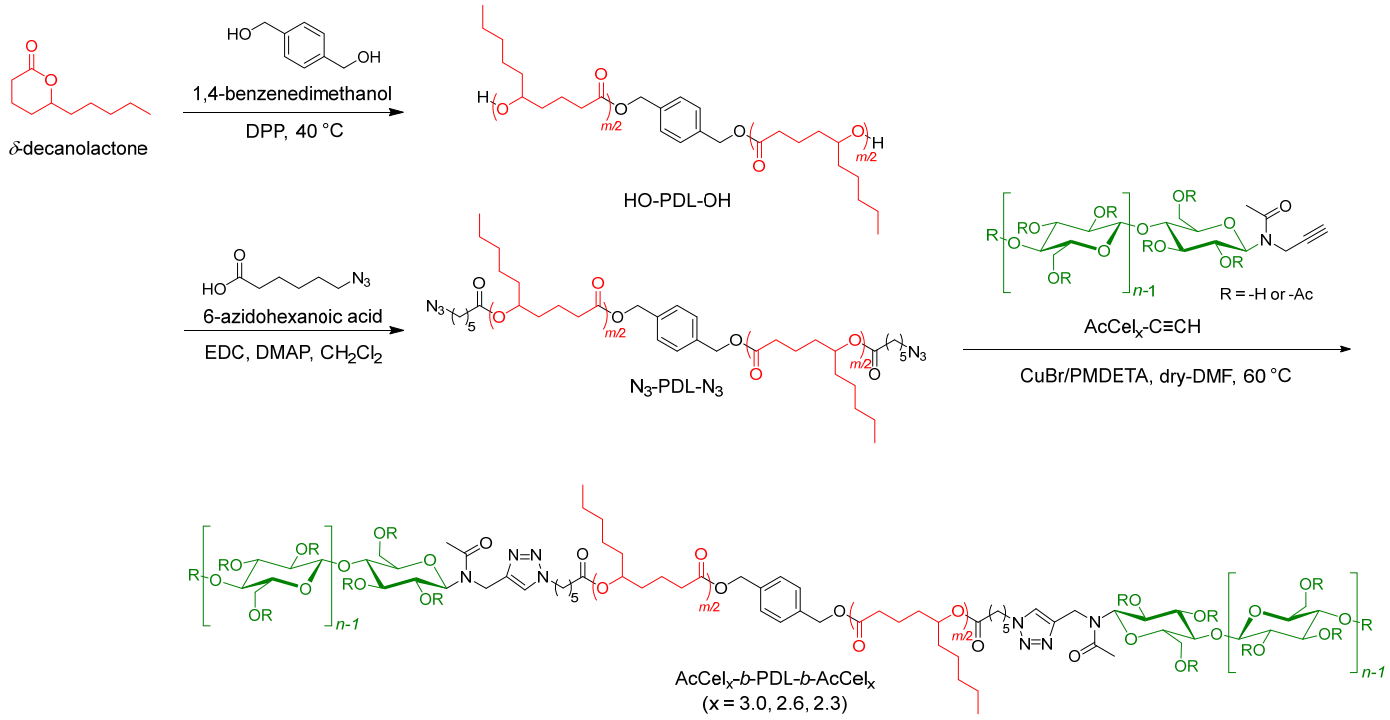
its inedible nature, the use of cellulose (and its derivatives) can avoid competition with the food supply. Although cellulose-based TPEs have potential as next-generation sustainable TPEs, challenges still exist in controlling and improving the material properties, such as microphase-separated structures, mechanical properties, thermal properties, and biodegradability, for practical applications.

An important factor in determining the physical properties of cellulose derivatives is the degree of substitution (DS). For example, good solvents for cellulose acetates depend on the DS. Cellulose triacetate (DS ≈ 3) is soluble in dichloromethane and chloroform ($CHCl_3$) but not in acetone and tetrahydrofuran (THF), whereas cellulose diacetate (DS ≈ 2) is soluble in acetone and THF (de Freitas, Senna, & Botaro, 2017). The DS also critically affects the hydrogen bonding profile. Native cellulose (DS = 0) is insoluble in common solvents because of its highly crystalline nature originating from strong inter- and intramolecular hydrogen bonds (Hata & Serizawa, 2021). Free hydroxy groups provide hydrogen bonding sites and increase polarity, which could positively affect the microphase separation and mechanical strength of cellulose acetate-based TPEs. The DS of cellulose acetate is also known to influence biodegradability. Cellulose triacetate does not biodegrade, but cellulose acetates with lower DSs (~2) biodegrade quickly, even in natural environments.(Edgar et al., 2001; Erdal & Hakkarainen, 2022; Kliem, Kreutzbruck, & Bonten, 2020; Puls, Wilson, & Hölter, 2011)

Thus, the material properties of cellulose-based TPEs can be improved and optimized by controlling the DS of the cellulose acetate block. In this study, we synthesized cellooligosaccharide acetate-*b*-PDL-*b*-cellooligosaccharide acetate ($AcCel_x$-*b*-PDL-*b*-$AcCel_x$, where x is the DS; x = 3.0, 2.6, and 2.3) triblock copolymers (**Scheme 1**). Cellooligosaccharide acetate blocks with three different DSs were used to investigate the influence of the DS on the microphase separation behavior and mechanical properties. Small-angle X-ray scattering (SAXS) and atomic force microscopy (AFM) revealed that $AcCel_x$-*b*-PDL-*b*-$AcCel_x$ tends to form more ordered microphase-separated structures as the DS decreases. Notably, $AcCel_{2.6}$-*b*-PDL-*b*-$AcCel_{2.6}$ and $AcCel_{2.3}$-*b*-PDL-

b-AcCel$_{2.3}$ exhibited superior mechanical properties to AcCel$_{3.0}$-*b*-PDL-*b*-AcCel$_{3.0}$. In addition, the biodegradability of AcCel$_x$-*b*-PDL-*b*-AcCel$_x$ in an aqueous environment was enhanced by decreasing the DS of the AcCel$_x$ segment. The findings of this study reveal that DS is an important factor for governing the properties of cellulose-based BCPs and demonstrate the potential of cellulose-derived TPEs as new sustainable materials.

Scheme 1. Synthesis of AcCel$_x$-*b*-PDL-*b*-AcCel$_x$



2. Experimental section

2.1. Materials

α-D-Glucose 1-phosphate disodium salt hydrate (αG1P, ≥97%), 4-(2-hydroxyethyl)-1-piperazineethanesulfonic acid (HEPES, ≥99.5%, titration), copper(I) bromide (CuBr, 99.999%), and 2,5-dihydroxybenzonoic acid (98%) were purchased from Sigma Aldrich and used as received. d(+)-cellobiose, sodium sulfate (Na_2SO_4, >99.0%), anhydrous magnesium sulfate ($MgSO_4$, >95%), propargylamine (>95%), acetic anhydride (>97%), hydrochloric acid (HCl, 35–37%), sulfuric acid (>96.0%), ethyl acetate (AcOEt, >99.3%), acetone (>99.0%), *N*,*N*-dimethylformamide (DMF, >99.0%), *N*,*N*-dimethylethanamide (DMAc, >99.0%), lithium chloride (LiCl, >99.0%), dry DMF (>99.5%; water content, <0.001%), dry toluene (>99.5%; water content, <0.001%), and dry CH_2Cl_2 (>99.5%; water content, <0.001%) were purchased from Kanto Chemical Co., Inc. and used as received. Dichloromethane (CH_2Cl_2, >99.0%), chloroform ($CHCl_3$, >99.0%), and methanol (MeOH, 99.6%) were purchased from Junsei Chemical Co., Ltd., and used as received. *N*,*N*,*N*′,*N*″,*N*″-Pentamethyldiethlenetriamine (PMDETA, >98.0%), diphenyl phosphate (DPP, >98.0%), 1,4-benzenedimethanol (BDM, >99.0%), 1-(3-dimethylaminopropyl)-3-ethylcarbodiimide hydrochloride (EDC·HCl, >98.0%), and 4-dimethylaminopyridine (DMAP, >99.0%) were purchased from Tokyo Chemical Industry Co., Ltd. (TCI) and used as received. δ-Decanolactone (δ-DL) was purchased from TCI and purified by distillation over CaH_2 under reduced pressure (6 Pa/112 °C). Dowex® 50WX2 hydrogen form was purchased from Sigma Aldrich and was washed with MeOH before use. Sucrose phosphorylase (SP) was purchased from Oriental Yeast Co., Ltd., and kept in a freezer after dissolved in Lysis buffer which composed of 20 mM tris(hydroxymethyl)aminomethane-HCl and 10 mM imidazole. Cellodextrin phosphorylase (CDP) (Hiraishi et al., 2009), 6-azidohexanoic acid (Grandjean et al., 2005), and ethynyl-functionalized cellobiose (CB−C≡CH) (Halila, S et al., 2008) were prepared according to previous reported methods.

2.2. Methods

^{1}H NMR measurement. ^{1}H NMR (400 MHz) spectra were obtained using a JEOL JNM-ECS 400 instrument at 25 °C. Note that ^{1}H NMR measurement of ethynyl-functionalized cellooligosaccharide (Cel−C≡CH) was performed at 55 °C.

Size exclusion chromatography (**SEC**). SEC measurements were performed at 40 °C in THF (flow rate, 1.0 mL min^{-1}) using a Jasco high-performance liquid chromatography system (PU-980 Intelligent HPLC Pump, CO-2065 Plus Intelligent Column Oven, RI-2031 Plus Intelligent RI Detector, and DG-2080-53 Degasser) equipped with a Shodex KF-G guard column (4.6 mm × 10 mm; particle size, 8 μm) and two Shodex KF-804L columns (linear; particle size 7 μm; 8.0 mm × 300 mm; exclusion limit, 4 × 10^4). The number-average molecular weight ($M_{n,SEC}$) and dispersity ($Đ$) were calculated based on polystyrene standards.

Fourie transform infrared spectroscopy (**FT-IR**). The FT-IR spectra were obtained using a PerkinElmer Frontier MIR spectrometer equipped with a single reflection diamond universal attenuated total reflection (ATR) accessory.

Differential scanning calorimetry (**DSC**) **measurement.** The DSC experiments were performed using a Hitachi DSC 7000X under nitrogen atmosphere. All polymer samples were heated to 240 °C, cooled to −100 or 30 °C, and heated again to 250 °C at the heating and cooling rate of 10 °C min^{-1}.

Thermogravimetric analysis (**TGA**). The TGA analysis was performed using Hitachi STA200RV under nitrogen atmosphere. All polymer samples were heated up to 550 °C at the heating rate of 10 °C min^{-1}.

Matrix-assisted laser desorption/ionization time-of-flight mass spectrometry (MALDI-TOF MS). The MALDI-TOF MS of the obtained products was performed using a Bruker Daltonick GmbsH Co., Inc. in the reflector mode controlled by the Flexcontrol 3.0 software package. For the Cel−C≡CH, the sample was prepared by mixing an ultrapure water dispersion of the compound (1.0

mg mL^{-1}, 200 μL), acetonitrile solution of a matrix (2,5-dihydroxybenzoic acid, 10 mg mL^{-1}, 100 μL), and trifluoroacetic acid (0.2% (v/v), 300 μL). A 1 μL aliquot of this mixture was loaded on a sample plate. For ethynyl-functionalized cellooligosaccharide acetate, the ethynyl-functionalized maltooligosaccharide, and ethynyl-functionalized maltooligosaccharide acetate, the samples were prepared by mixing a THF solution of the compound (5 mg mL^{-1}, 100 μL) and a matrix (2,5-dihydroxybenzoic acid, 10 mg mL^{-1}, 500 μL). A 1 μL aliquot of this mixture was loaded was loaded on a sample plate, which was coated by an acetone solution of NaI (1 μL, 1 mmol L^{-1}) as the cationic agent.

Atomic force microscopy (AFM) observation. The AFM phase images were obtained using a Molecular Imaging PicoPlus atomic force microscope operating in the tapping mode with a silicon cantilever (Nanoworld AG, NANOSENSORS^{TM} PPP-NCH) having resonant frequency and spring constant of 190 kHz and 48 N m^{-1}, respectively. The thin film samples for the AFM observation were prepared by spin-coating (1,500 rpm for 60 s) the polymer solution in $CHCl_3$ (1 wt%) onto a Si substrate with a native oxide layer.

Scanning electron microscope (SEM). The samples were mounted on a brass stub put conductive carbon tape and coated gold particle by ion sputtering for 1 min at 15 mA using a Hitachi E-1010. The sample observations were conducted using a JEOL JSM-7001FA scanning electron microscope at an accelerating voltage of 5kV.

Small-angle X-ray scattering (SAXS) and wide-angle X-ray diffraction (WAXD). The SAXS and WAXD measurements of the obtained polymers were performed at the BL-6A or BL-10C beamline of the Photon Factory in the High Energy Accelerator Research Organization (KEK, Tsukuba, Japan) using X-ray beams with λ = 0.15 nm at room temperature. The scattering data were collected by a 2D detector (PILATUS3 1M or 2M (SAXS) (Dectris Ltd.); PILATUS3 100K or 200K (WAXD) (Dectris Ltd.)), where the samples-to-detector distance was set to be 1.5 m and 0.2 m for SAXS and WAXD measurement, respectively. The scattering angle (θ) was calibrated using silver behenate (Nagara Science Co., Ltd) as the standard and derived the scattering vector (q) from

Bragg's equation ($|q| = (4\pi/\lambda)\sin(\theta/2)$). The domain-spacing ($d$) value was calculated by $d = 2\pi/|q^*|$ ($|q^*|$ is principal scattering peak position). The polymer films or powders were sandwiched by two pieces of Kapton tapes with a spacer of a stain less washer, which were applied for the measurement.

Tensile testing. The tensile tests were performed with an 34SC-1 (INSTRON) tensile tester at the temperature of 20 °C and the humidity of 45%. The film samples for the tensile tests were prepared by casting the polymer solutions from the $CHCl_3$ (15 mL) on a Teflon dish and drying at r.t. for 2 d followed by vacuum drying at r.t. for 2 d. The obtained elastic films were cut into a dog bone shape of 12 × 2 × ca. 0.13 mm (Japanese Industrial Standards (JIS) K6251). For each film, three samples were tested and the average values of the elastic modulus, strain at break, stress at break, and toughness were calculated. The crosshead speed applied during the measurements was 10 mm min^{-1}. The strain at break was taken as the engineering strain where the stress drops suddenly.

Biodegradation test. Biodegradation test was conducted in freshwater closed recirculating aquaculture system (RAS) rearing the Nile tilapia *Oreochromis niloticus* where samples cut into 1 cm squares were put in polyethylene net (**Fig. 1**). The temperature of 200-L fish tank was controlled at 26 °C by heater. Dissolved oxygen level was maintained at saturation （~8 mg/L） by aeration.

To maintain the water quality for rearing fish healthy, a 45-L down hanging sponge (DHS) reactor with the flow rate of 600 L/h by water pump was equipped for nitrification of ammonia nitrogen. Fish density of RAS in this study was approximately 4 kg fish/kL. The 900 CFU/mL bacteria in the water of RAS was detected using culture medium for determining a total viable cell count, Compact dry (Nissui Pharmaceutical Co., Ltd.). Pictures of samples were taken with a digital camera (Floyd 4K, Wraymer, Japan) installed on a stereo microscope (SZX10, Olympus, Japan) in once a week. After the biodegradation test, the samples were washed pure water and lyophilized for 1 day.

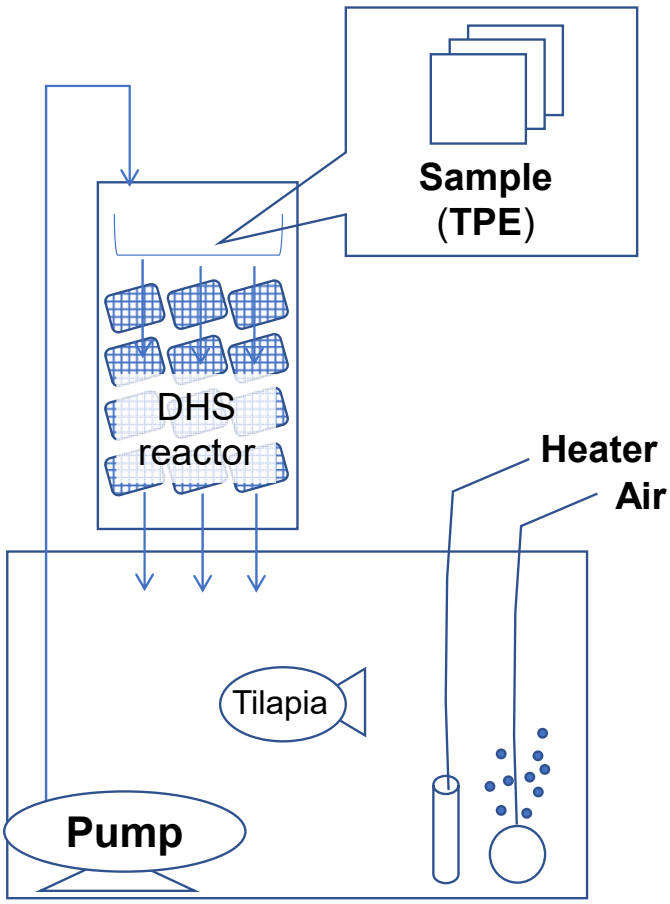
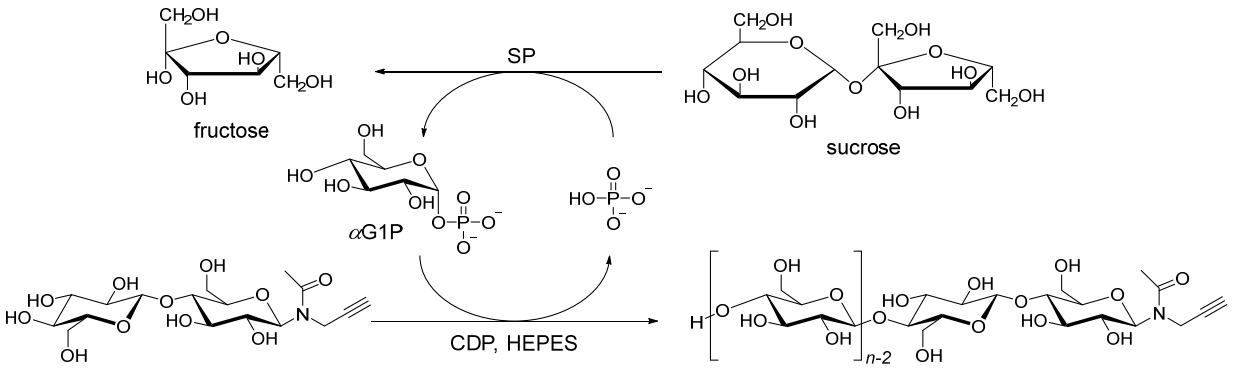


Fig. 1. Schematic images of the recirculating aquaculture system (RAS) used in this study.

2.3. Synthesis details

Synthesis of ethynyl-functionalized cellooligosaccharide (Cel−C≡CH) using CDP and SP

Scheme 2. Synthesis of Cel−C ≡ CH



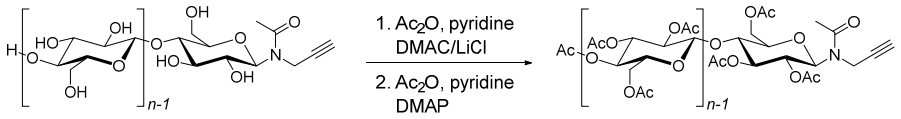
10 mM *α*G1P, 50 mM CB−C≡CH, and 500 mM sucrose were incubated with 50 μg mL^{-1} CDP and 5 U mL^{-1} SP in 50 mM HEPES buffer solutions (pH 7.5, 104 mL, divided into 11 centrifuge tubes) at 40 °C. After incubating for 7 days, the reaction mixtures were centrifuged to isolate the insoluble product and the resulting pellet was washed with water followed by centrifugation at 14,000 rpm for 20 min at 4 °C several times to give swollen Cel−C≡CH. The aliquot of the obtained product was freeze-dried in vacuo for 2 days to give white powder (6.68 g). Yield: 58.4%.

$M_{n,NMR}$ = 1,170 g mol^{-1}, $M_{n,MALDI}$ = 1,210 g mol^{-1}.

^{1}H NMR (400 MHz, 10% (w/w) NaOD-D_2O): *δ* (ppm) 5.59–5.42, 4.55–4.32 (2x m, rotamers 1H, −C*H*N(Ac)−), 4.15 (d, *J* = 8.0 Hz, 1H × (*n*−1), *H*-1^{Cel}), 4.06–2.67 (m, 9H × *n* + 3H, *H*-2, -3, -4, -5, -$6^{Cel n}$, O*H*$^{Cel n}$, −N(Ac)CH_2−), 2.53–2.45, 2.32–2.17 (m, rotamers, 1H, −CC*H*), 1.67–1.55 (m, 3H, −N(C=O)CH_3).

Synthesis of ethynyl-functionalized cellooligosaccharide triacetate ($AcCel_{3.0}$−C≡CH)

Scheme 3. Synthesis of $AcCel_{3.0}$−C ≡ CH

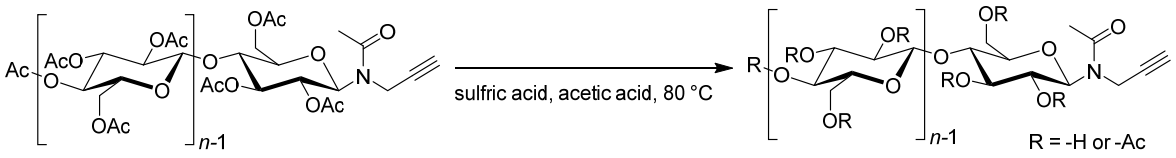


Cel_n-C≡CH $AcCel_n$-C≡CH

Wet Cel_n−C≡CH (6.28 g, by dry weight) was dispersed in acetone and centrifuged twice (7,000 rpm/30 min/0 °C, 7,000 rpm/15 min/0 °C). The pellet was dispersed in acetone (300 mL) and stirred over night at room temperature. After the centrifugation (7,000 rpm/15 min/0 °C), the pellet was washed with DMAc followed by centrifugation (7,000 rpm/15 min/0 °C). The pellet was dispersed in DMAc (250 mL) and stirred at r.t. After 3 h, LiCl (4.02 g, 94.8 mmol) was added to the mixture and kept stirring over-night. After adding a solution of acetic anhydride in pyridine (1/1 (v/v), 40 mL), the mixture was stirred 5 d. The reaction mixture was diluted with CH_2Cl_2 and washed with 1M HCl (100 mL) three times. The organic layer was dried over $MgSO_4$ and concentrated to give a white solid. The obtained solid and DMAP (139.6 mg, 1.14 mmol) was added to a solution of acetic anhydride in pyridine (1/2 (v/v), 120 mL) and stirred at r.t. for 3 d. After removing the solvent by evaporation, the residue was dissolved in ethyl acetate and washed with 1 M HCl and saturated $NaHCO_3$ solutions. After the organic layer was dried over Na_2SO_4 and concentrated by evaporation, the residue was dissolved with a little of CH_2Cl_2 and poured into the cold-MeOH. The precipitated product was dried under vacuo to give $AcCel_{3.0}$−C≡CH as a white solid (6.68 g). Yield: 55.7%. $M_{n,NMR}$ = 2,080 g mol^{-1}, $M_{n,MALDI}$ = 2,360 g mol^{-1}, $M_{n,SEC}$ = 2,560 g mol^{-1} (THF), $Đ$ = 1.06 (THF). ^{1}H NMR (400 MHz, DMSO-d_6): δ (ppm) 6.09 (d), 5.88−5.74 (m) (2x, 1H, rotamers, −C*H*N(Ac)−), 5.53−3.22 (m, 7H × (n−1) + 8H, *H*-1, -2, -3, -4, -5, -6^{AcCel_n} of anhydro glucose repeating unit and non-reducing terminal end group, −N(Ac)CH_2−), 2.70−2.63 (m, 1H, −CC*H*), 2.34−1.64 (m, 9n+6, CH_3-Ac^{AcCel_n}, −N(C=O)CH_3).

Deacetylation of $AcCel_{3.0}$–C≡CH

Scheme 4. Deacetylation of $AcCel_{3.0}$–C ≡ CH



Synthesis of $AcCel_{2.6}$–C≡CH

Typical deacetylation procedure is as follows (Method A): $AcCel_{3.0}$–C≡CH (1.49 g, 645 μmol, $M_{n,MALDI}$ = 2,310, $Đ$ = 1.07) was dissolved in acetic acid (25 mL) in a round-bottom flask. Concentrated sulfuric acid (410 μL) was added slowly to the solution followed by water (2.5 mL), and while the mixture was stirred at 80 °C. After 9.5 min, water was added to the mixture to precipitate the product. The precipitate was filtered and washed several times using water. After drying under reduced pressure, the cellooligosaccharide acetate with degree of the substitution (DS) of 2.6 was obtained as a white powder (1.33 g). Note that the DS of cellooligosaccharide acetate was labeled as subscript number, i.e., $AcCel_x$–C≡CH (x means the DS).

Yield: 95.1%

See **Fig. S7** for ^{1}H NMR spectrum.

Synthesis of $AcCel_{2.3}$–C≡CH

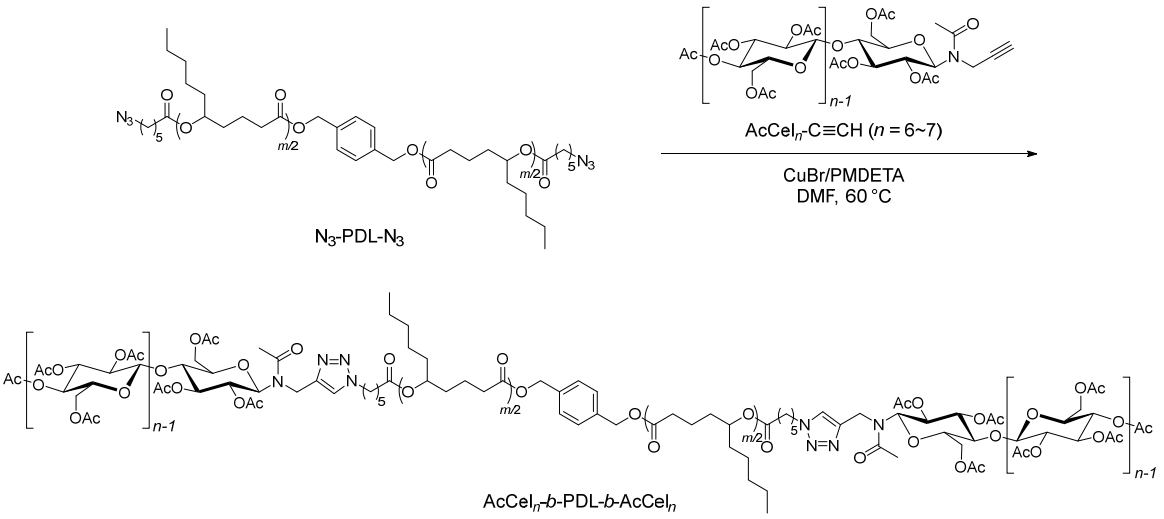
The method A was used for the deacetylation of $AcCel_{3.0}$–C≡CH (1.50 g, 649 μmol, $M_{n,MALDI}$ = 2,310, $Đ$ = 1.07) with acetic acid (25 mL), concentrated sulfuric acid (410 μL), and water (2.5 mL) for 20 min to synthesize $AcCel_{2.3}$–C≡CH with the DS of 2.3 (1.01 g).

Yield: 75.1%

See **Fig. S7** for ^{1}H NMR spectrum.

Synthesis of ABA-type BCP consisting of cellooligosaccharide acetate and PDL (AcCel$_x$-*b*-PDL-*b*-AcCel$_x$) via click reaction

Scheme 5. Synthesis of AcCel$_x$-*b*-PDL-*b*-AcCel$_x$



Synthesis of AcCel$_{3.0}$-*b*-PDL-*b*-AcCel$_{3.0}$

A typical click reaction procedure is as follows (Method B): A degassed solution of N_3−PDL−N_3 ($M_{n,NMR}$ = 17,800 g mol^{-1}, 1.43 g, 80.3 μmol) and PMDETA (37.8 μL, 181 μmol) in dry DMF (20 mL) was transferred to a Schlenk tube in which AcCel$_n$–C≡CH (425.1 mg, 184 μmol) and CuBr (27.7 mg, 193 μmol) were placed. The mixture was stirred for 43 h at 60 °C under an argon atmosphere. After cooling to room temperature, Dowex® 50WX2 and a few drops of water were added to remove Cu catalyst. The unreacted AcCel$_{3.0}$–C≡CH was removed by the preparative SEC in $CHCl_3$ to give AcCel$_{3.0}$-*b*-PDL-*b*-AcCel$_{3.0}$ as a pale-yellow elastic material (1.18 g). Yield: 65.6%.

$M_{n,SEC}$ = 27,700 g mol^{-1} (THF), $Đ$ = 1.03 (THF), $M_{n,total}$= 22,400 g mol^{-1}.

See **Fig. S10** for ^{1}H NMR spectrum.

Synthesis of $AcCel_{2.6}$-*b*-PDL-*b*-$AcCel_{2.6}$

The Method B was used for the click reaction of N_3−PDL−N_3 ($M_{n,NMR}$ = 17,800 g mol^{-1}, 1.60 g, 89.9 μmol) and $AcCel_n$−C≡CH (444.6 mg, 204 μmol) in dry DMF (20 mL) with CuBr (28.1 mg, 196 μmol) and PMDETA (41.3 μL, 198 μmmol) to synthesize $AcCel_{2.6}$-*b*-PDL-*b*-$AcCel_{2.6}$. The crude product was purified by reprecipitation to give $AcCel_{2.6}$-*b*-PDL-*b*-$AcCel_{2.6}$ as a white elastic material (1.19 g). Yield: 59.6%.

$M_{n,SEC}$ = 30,200 g mol^{-1} (THF), $Đ$ = 1.04 (THF), $M_{n,total}$= 22,200 g mol^{-1}.

See **Fig. S11** for ^{1}H NMR spectrum.

Synthesis of $AcCel_{2.3}$-*b*-PDL-*b*-$AcCel_{2.3}$

The Method B was used for the click reaction of N_3−PDL−N_3 ($M_{n,NMR}$ = 17,800 g mol^{-1}, 1.40 g, 78.7 μmol) and $AcCel_n$−C≡CH (372.5 mg, 178 μmol) in dry DMF (20 mL) with CuBr (27.0 mg, 188 μmol) and PMDETA (37.8 μL, 181 μmol). The crude product was purified by reprecipitation to give $AcCel_{2.3}$-*b*-PDL-*b*-$AcCel_{2.3}$ as a white elastic material (1.19 g). Yield: 68.8%.

$M_{n,SEC}$ = 26,500 g mol^{-1} (THF), $Đ$ = 1.04 (THF), $M_{n,total}$= 22,000 g mol^{-1}.

See **Fig. S12** for ^{1}H NMR spectrum.

3. Results and discussion

3.1. Cellooligosaccharide preparation

We first investigated the improved synthesis of propargyl-functionalized cellooligosaccharide (Cel–C≡CH), a precursor of cellooligosaccharide triacetate, through enzymatic polymerization (**Scheme 2**; Hiraishi et al., 2009; Katsuhara et al., 2021; Kuga, Sunagawa, & Igarashi, 2022; Petrović, Kok, Woortman, Ćirić, & Loos, 2015; Pylkkänen et al., 2020; Serizawa, Kato, Okura, Sawada, & Wada, 2016; Sugiura, Sawada, Tnaka, & Serizawa, 2021; Sugiura, Saito, Sawada, Tanaka, & Serizawa, 2022). In our previous report, we prepared Cel–C≡CH mainly consisting of 6–8-mers through the cellodextrin phosphorylase (CDP)-mediated oligomerization of *α*-D-glucose-1-phosphate (*α*G1P) in the presence of *N*-acetyl-propargyl D-(+)-cellobiose as a primer. Cellooligosaccharides with various functional groups at the reducing end and narrow dispersities (*Đ*) were easily obtained using CDP-mediated oligomerization. However, low product yields (~20%) were observed (Katsuhara et al., 2021), likely because phosphoric acid was also produced, which promoted the reverse reaction (i.e., phosphorolysis of the cellooligosaccharide). To improve the product yield, we modified the enzyme polymerization system to avoid the accumulation of phosphoric acid. Sucrose and sucrose phosphorylase were added to the previous system (Katsuhara et al., 2021) to simultaneously reuse the generated phosphoric acid and produce *α*G1P from sucrose (for details, see Supporting Information (SI)). Consequently, the yield of Cel–C≡CH reached ~60%, which is three times greater than that achieved with our previous protocol (~20%). The characterization data for the obtained Cel–C≡CH are shown in **Fig. S1**. The ^{1}H NMR signals were assigned to the expected structure and a number-averaged degree of polymerization (DP) of 6.59 was calculated, which corresponds to a number-averaged molecular weight ($M_{n,NMR}$) of 1,170 g mol^{-1}. Matrix-assisted laser desorption/ionization time-of-flight mass spectrometry (MALDI-TOF MS) analysis revealed two series of repeating peaks separated by 162 Da in the range of 900–1,500 Da. The major and minor series of peaks are consistent with the Na^+ and K^+ adducts, respectively, of Cel–C≡CH comprising 6–8-mers. The number-averaged molecular weight estimated from the

MALDI-TOF MS analysis ($M_{n,MALDI}$) was 1,210 g mol^{-1}, which is similar to the $M_{n,NMR}$ value (1,170 g mol^{-1}).

The fully acetylated propargyl-functionalized cellooligosaccharide (i.e., celloologosaccharide triacetate (AcCel$_{3.0}$–C≡CH)) was prepared according to the established procedure (**Scheme 3**; Kamitakahara, Enomoto, Hasegawa, & Nakatsubo, 2005; Katsuhara et al., 2021). The $M_{n,MALDI}$ value of the synthesized AcCel$_{3.0}$–C≡CH (2,310 g mol^{-1}; **Fig. S2**) in this study was slightly larger than that of our previously reported AcCel$_{3.0}$–C≡CH ($M_{n,MALDI}$ = 2,120 g mol^{-1}; **Fig. S3**). As revealed by MALDI-TOF MS analysis, AcCel$_{3.0}$–C≡CH synthesized in this work exhibited repeating peaks corresponding to 6–11-mers, whereas our previous sample exhibited repeating peaks corresponding to 6–9-mers (**Fig. S3**) (Katsuhara et al., 2021). This result was further supported by size-exclusion chromatography (SEC) measurements, with the M_n determined by SEC ($M_{n,SEC}$) for AcCel$_{3.0}$–C≡CH ($M_{n,SEC}$ = 2,560 g mol^{-1}) synthesized in this study being larger than that of the previous sample ($M_{n,SEC}$ = 2,180 g mol^{-1}) (**Fig. S4**).

Next, the partial deacetylation of AcCel$_{3.0}$–C≡CH was performed in the presence of sulfuric acid to obtain cellooligosaccharide acetates with various DSs (**Scheme 4**; Cerqueira, Valente, Filho, & Burrows, 2009; Kono, Hashimoto, & Shimizu, 2015; Tezuka & Tsuchiya, 1995). We found that the DS could be easily controlled between 3.0 and 2.3 by varying the reaction time. AcCel$_{2.6}$–C≡CH and AcCel$_{2.3}$–C≡CH were obtained by hydrolyzing for 9.5 and 20 min, respectively (for details, see the Supporting Information (SI) and **Figs. S5–S7**). The DS of the product was determined by comparing the ^{1}H NMR signal intensities for the protons of the acetyl groups and glycosidic ring. Importantly, the propargyl group at the reducing end remained intact during deacetylation, as evidenced by the minor ^{1}H NMR signal of the methylidyne proton at ~2.88 ppm (**Fig. S7**a). In addition, the intensity of the IR absorption band at ~3,500 cm^{-1} corresponding to hydroxy groups increased when the DS decreased (**Fig. S7**b), which is consistent with the generation of more hydroxy groups as deacetylation proceeds. The MALDI-TOF MS spectra of AcCel$_{2.6}$–C≡CH and AcCel$_{2.3}$–C≡CH exhibited a series of repeated peaks that differed by ~42 Da

from the signals of $AcCel_{3.0}$–C≡CH (**Figs. S5** and **S6**), which corresponds to the difference in molecular mass between the acetoxy group (OAc, 59.01 Da) and the hydroxy group (OH, 17.00 Da). These results indicate that the deacetylation of $AcCel_{3.0}$–C≡CH proceeded, while the ethynyl group was maintained. Thus, we successfully synthesized three $AcCel_x$–C≡CH samples with different DSs but similar M_n and $Đ$ values (~2,000 g mol^{-1} and 1.07, respectively) (**Fig. S7**c).

3.2. BCP synthesis

To synthesize the target BCPs ($AcCel_{3.0}$-*b*-PDL-*b*-$AcCel_{3.0}$, $AcCel_{2.6}$-*b*-PDL-*b*-$AcCel_{2.6}$, and $AcCel_{2.3}$-*b*-PDL-*b*-$AcCel_{2.3}$), in which the DS of the cellooligosaccharide acetate block varies, an *α*,*ω*-diazido-functionalized PDL (N_3–PDL–N_3; $M_{n,NMR}$ = 17,800 g mol^{-1}, $Đ$ = 1.05) was synthesized according to our established procedure (Isono, Nakahira, et al., 2020; Isono, Ree, Tajima, Borsali, & Satoh, 2018; Katsuhara et al., 2021) (for details, see the SI, **Schemes S1** and **S2**, and **Figs. S8** and **S9**). A copper-catalyzed azido-alkyne click reaction between N_3–PDL–N_3 and the $AcCel_x$–C≡CH samples produced the target BCPs in 60–70% isolated yield (**Scheme 5**). After the click reaction, the reaction mixture was treated with a cation exchange resin and then reprecipitated in MeOH to afford the BCP. However, in the case of $AcCel_{3.0}$-*b*-PDL-*b*-$AcCel_{3.0}$, unreacted $AcCel_{3.0}$–C≡CH could not be removed by reprecipitation because of its poor solubility in MeOH. As we were unable to find a solvent that selectively dissolved $AcCel_{3.0}$–C≡CH while precipitating BCP, unreacted $AcCel_{3.0}$–C≡CH was removed by preparative SEC, which afforded $AcCel_{3.0}$-*b*-PDL-*b*-$AcCel_{3.0}$ in 65.6% yield. In contrast, unreacted $AcCel_{2.6}$–C≡CH and $AcCel_{2.3}$–C≡CH were easily removed by simple reprecipitation in MeOH, giving $AcCel_{2.6}$-*b*-PDL-*b*-$AcCel_{2.6}$ and $AcCel_{2.3}$-*b*-PDL-*b*-$AcCel_{2.3}$ in 95.1% and 75.1% yield, respectively. This behavior suggests that the reduced DSs of $AcCel_{2.6}$–C≡CH and $AcCel_{2.3}$–C≡CH impart improved solubility in polar solvents such as MeOH.

FT-IR spectroscopy confirmed that each click reaction proceeded quantitatively, as the absorption band at ~2,100 cm^{-1} derived from azido groups disappeared completely. The ^{1}H NMR

spectra of the products exhibited proton signals corresponding to $AcCel_x$ (5.4–3.0 ppm) and PDL moieties (5.0–4.7, 2.6–0.7 ppm) as well as triazole rings (~7.4 and 7.3 ppm) (**Figs. S10**–**12**). Moreover, SEC elution peaks appeared at higher molecular weights than for N_3–PDL–N_3 while maintaining a unimodal shape, and no elution peak corresponding to unreacted $AcCel_x$–C≡CH was observed (**Fig. S13**). Collectively, these results support the successful synthesis of the target BCPs. The detailed characteristics (molecular weight, $Đ$, volume fraction of PDL segments (f_{PDL})) of $AcCel_{3.0}$-*b*-PDL-*b*-$AcCel_{3.0}$, $AcCel_{2.6}$-*b*-PDL-*b*-$AcCel_{2.6}$, and $AcCel_{2.3}$-*b*-PDL-*b*-$AcCel_{2.3}$ are summarized in **Table 1**.

Table 1. Molecular characteristics of $AcCel_x$-*b*-PDL-*b*-$AcCel_x$

Polymer	M_n	$M_{n,SEC}$[e]	$Đ$[e]	$T_{g,PDL}$[f] [°C]	$T_{g,AcCel}$[f] [°C]	f_{PDL}[h]
$AcCel_{3.0}$–C≡CH	2,310[a]	2,560	1.06	-	110	-
$AcCel_{2.6}$–C≡CH	2,180[b]	2,590	1.06	-	116	-
$AcCel_{2.3}$–C≡CH	2,090[b]	2,590	1.06	-	121	-
N_3–PDL–N_3	17,800[c]	22,000	1.04	−58	-	-
$AcCel_{3.0}$-*b*-PDL-*b*-$AcCel_{3.0}$	22,400[d]	27,700	1.03	−55	n.d.[g]	0.79
$AcCel_{2.6}$-*b*-PDL-*b*-$AcCel_{2.6}$	22,200[d]	28,400	1.04	−56	n.d.[g]	0.80
$AcCel_{2.3}$-*b*-PDL-*b*-$AcCel_{2.3}$	22,000[d]	27,600	1.04	−57	n.d.[g]	0.81

[a]Determined by MALDI-TOF MS. [b]Calculated as M_n of $AcCel_{3.0}$–C≡CH − (3 − DS) × (M_n of an acetyl group (43.05) − atomic weight of H (1.01)) × DP. [c]Determined by ^{1}H NMR spectroscopy in $CDCl_3$. [d]Caluculated from the M_n values $AcCel_x$–C≡CH and N_3–PDL–N_3. [e]Determined by SEC in THF using PS standards. [f]Determined using DSC at a heating rate of 10 °C min^{-1}. [g]Not determined. [h]Calculated using the density of each block: 1.29 g cm^{-3} for $AcCel_x$−C≡CH and 0.97 g cm^{-3} for PDL.

3.3. Thermal properties

Thermal properties, such as the T_g and degradation temperature, are critical characteristics for elastomer applications. Thus, we investigated the thermal properties of the $AcCel_x$-*b*-PDL-*b*-$AcCel_x$ samples and their constituent blocks using differential scanning calorimetry (DSC) and thermogravimetric analysis (TGA) under a N_2 atmosphere. DSC analysis of $AcCel_x$–C≡CH with different DSs revealed an increase in T_g ($T_{g,AcCel}$) with decreasing DS (110, 116, and 121 °C for DS = 3.0, 2.6, and 2.3; **Figs. 2**a–c). This behavior is attributed to an increase in molecular interactions through hydrogen bonding as DS decreases, which results in decreased chain mobility (Kamide &

Saitohal, 1985). The DSC curves of AcCel$_x$-*b*-PDL-*b*-AcCel$_x$ during the second heating process exhibited a baseline shift at approximately −55 °C corresponding to the T_g of the PDL segment ($T_{g,PDL}$; **Figs. 2**d–f and **S14**). The T_g of AcCel$_x$ ($T_{g,AcCel}$) was not clearly observed because of the small volume fraction of this segment in the BCPs ($f_{AcCelx} \approx 0.2$).

TGA analysis revealed a 5% weight-loss temperature ($T_{d5\%}$) of ~300 °C for the synthesized BCPs, AcCel$_x$–C≡CH, and N_3–PDL–N_3, which ensures sufficient thermal stability (**Figs. S15** and **S16**). Notably, during heating, the BCP films and AcCel$_x$–C≡CH powders underwent a solid–liquid transformation at 160–200 °C (**Fig. S16**), indicating that the BCPs are thermoplastic in nature, which is favorable for potential TPE applications.

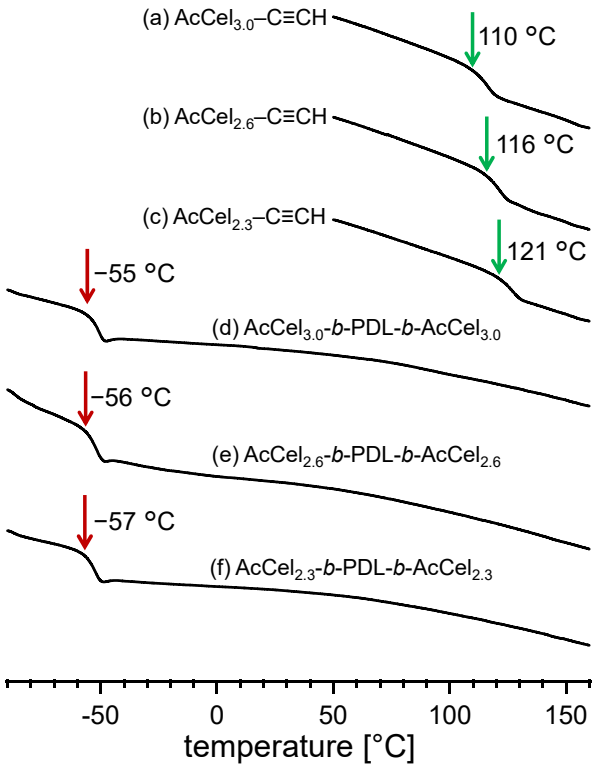


Fig. 2. DSC curves of (a) AcCel$_{3.0}$–C≡CH, (b) AcCel$_{2.6}$–C≡CH, (c) AcCel$_{2.3}$–C≡CH, (d) AcCel$_{3.0}$-*b*-PDL-*b*-AcCel$_{3.0}$, (e) AcCel$_{2.6}$-*b*-PDL-*b*-AcCel$_{2.6}$, and (f) AcCel$_{2.3}$-*b*-PDL-*b*-AcCel$_{2.3}$ during the second heating process.

3.4. Microphase separation

Microphase-separated structures are known to affect the mechanical properties of TPEs. Therefore, SAXS measurements were performed to clarify the nanostructures of AcCel$_x$-*b*-PDL-*b*-AcCel$_x$ in the bulk state. Bulk film samples were prepared by solvent casting from a $CHCl_3$ solution, drying at atmospheric pressure for 2 days, and then vacuum drying at room temperature for 2 days. Subsequently, the films of AcCel$_{3.0}$-*b*-PDL-*b*-AcCel$_{3.0}$ and AcCel$_{2.6}$-*b*-PDL-*b*-AcCel$_{2.6}$ were thermally annealed at 150 °C for 6 h under vacuum. On the other hand, the film of AcCel$_{2.3}$-*b*-PDL-*b*-AcCel$_{2.3}$ was annealed at 180 °C for 6 h because the T_g of AcCel$_{2.3}$–C≡CH was a little higher than that of AcCel$_{3.0}$–C≡CH and AcCel$_{2.6}$–C≡CH. The SAXS profiles of the AcCel$_x$-*b*-PDL-*b*-AcCel$_x$ films without thermal annealing exhibited only a primary scattering peak, implying ill-defined nanostructures (**Fig. 3**).

AcCel$_{3.0}$-*b*-PDL-*b*-AcCel$_{3.0}$ did not form ordered microphase-separated structures, even after thermal annealing, as indicated by the sole primary scattering peak in the SAXS profile. In contrast, the wide-angle X-ray diffraction (WAXD) profile of annealed AcCel$_{3.0}$-*b*-PDL-*b*-AcCel$_{3.0}$ showed sharp scattering peaks assignable to cellulose triacetate I crystals (**Fig. S17**). Initially, we expected that AcCel$_{3.0}$-*b*-PDL-*b*-AcCel$_{3.0}$ would have an ordered body-centered cubic (BCC) spherical morphology, as observed previously for a BCP with a comparable composition and molecular weight (Katsuhara et al., 2021). However, the M_n of the AcCel$_{3.0}$ segment in the present AcCel$_{3.0}$-*b*-PDL-*b*-AcCel$_{3.0}$ was slightly higher than that in the previous BCP, which greatly affected the crystallization ability, as evidenced by the WAXD analysis of AcCel$_{3.0}$–C≡CH (**Fig. S18**). The nanostructures of semicrystalline BCPs are known to be influenced by the interplay between the driving forces for crystallization and microphase separation (He & Xu, 2012). The strong tendency of AcCel$_{3.0}$–C≡CH to crystallize owing to its higher M_n could interfere with microphase separation, resulting in the ill-defined nanostructures observed for AcCel$_{3.0}$-*b*-PDL-*b*-AcCel$_{3.0}$. Considering the large effect of M_n on the crystallization ability of AcCel$_{3.0}$, this unique phenomenon requires further investigation in the future.

The SAXS profiles of the annealed AcCel$_{2.6}$-*b*-PDL-*b*-AcCel$_{2.6}$ and AcCel$_{2.3}$-*b*-PDL-*b*-AcCel$_{2.3}$ films exhibited multiple scattering peaks assignable to BCC spherical structures, whereas the WAXD profiles showed only amorphous halos. The intersphere distances ($d_{S\text{-}S,SAXS}$) of AcCel$_{2.6}$-*b*-PDL-*b*-AcCel$_{2.6}$ and AcCel$_{2.3}$-*b*-PDL-*b*-AcCel$_{2.3}$ were calculated to be 14.8 and 15.1 nm, respectively ($d_{S\text{-}S,SAXS} = (2\pi/q^*)(3/2)^{1/2}$), where the q^* is the primary scattering peak position). Interestingly, AcCel$_{2.6}$-*b*-PDL-*b*-AcCel$_{2.6}$ and AcCel$_{2.3}$-*b*-PDL-*b*-AcCel$_{2.3}$ exhibited different *d* values despite their comparable molecular weights and volume fractions. The *d* value of a microphase-separated structure is known to reflect the Flory–Huggins interaction parameter (χ), as follows:(Zhou, Janes, Kim, Willson, & Ellison, 2016)

$$d = a\chi^{1/6}N^{2/3} \quad (1)$$

where *a* is a constant related to the statistical chain length. Eq. (1) demonstrates that *d* increases with χ. Assuming that AcCel$_{2.6}$-*b*-PDL-*b*-AcCel$_{2.6}$ and AcCel$_{2.3}$-*b*-PDL-*b*-AcCel$_{2.3}$ have the same *a* and *N* values, a $\chi_{AcCel2.3}/\chi_{AcCel2.6}$ value of 1.13 can be determined based on eq. (1) and the $d_{S\text{-}S,SAXS}$ values of AcCel$_{2.3}$-*b*-PDL-*b*-AcCel$_{2.3}$ (15.1 nm) and AcCel$_{2.6}$-*b*-PDL-*b*-AcCel$_{2.6}$ (14.8 nm). This result indicates that reducing the DS of the AcCel$_x$ segments increases the χ value, leading to ordered microphase-separated structures.

AFM was used to visualize the microphase-separated structures in the AcCel$_x$-*b*-PDL-*b*-AcCel$_x$ thin films (**Fig. 4**). Thin film samples were prepared by spin-coating a $CHCl_3$ solution (1 wt%) of AcCel$_x$-*b*-PDL-*b*-AcCel$_x$ on bare Si substrates. The AFM phase images of AcCel$_x$-*b*-PDL-*b*-AcCel$_x$ before thermal annealing exhibited ill-ordered dotted patterns, consistent with the observation of a single primary scattering peak in the SAXS profiles of the non-annealed BCPs. Interestingly, the AFM image of the AcCel$_{3.0}$-*b*-PDL-*b*-AcCel$_{3.0}$ thin film showed fiber-like structures after thermal annealing, which could be related to the high crystallinity of the AcCel$_{3.0}$ segment. Few such fiber-like structures were observed in the previously synthesized AcCel$_{3.0}$-*b*-PDL-*b*-AcCel$_{3.0}$ with a comparable composition (Katsuhara et al., 2021). This result indicates that the driving force for crystallization was stronger than that for microphase separation in the present

AcCel$_{3.0}$–C≡CH sample with a higher M_n, resulting in the formation of an ill-ordered fiber-like pattern rather than an ordered microphase-separated structure. In contrast, the AFM phase images of the thermally annealed AcCel$_{2.6}$-*b*-PDL-*b*-AcCel$_{2.6}$ and AcCel$_{2.3}$-*b*-PDL-*b*-AcCel$_{2.3}$ thin films exhibited highly ordered dotted patterns, reflecting a BCC structure. The intersphere distances calculated from the fast Fourier transform (FFT) images ($d_{S\text{-}S,AFM}$) of the AcCel$_{2.6}$-*b*-PDL-*b*-AcCel$_{2.6}$ and AcCel$_{2.3}$-*b*-PDL-*b*-AcCel$_{2.3}$ films were 13.0 and 13.1 nm, respectively, which are similar to the $d_{S\text{-}S,SAXS}$ values.

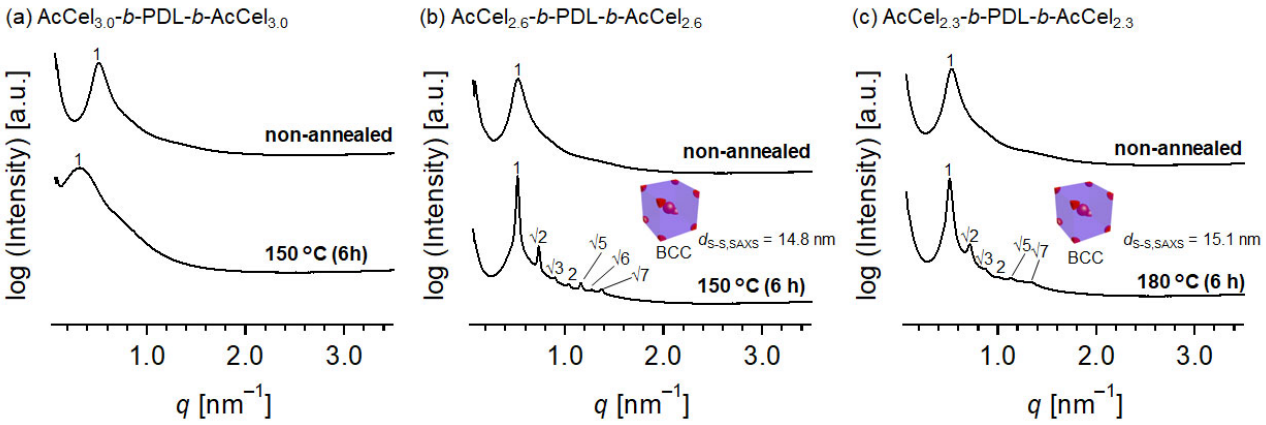


Fig. 3. SAXS profiles of (a) AcCel$_{3.0}$-*b*-PDL-*b*-AcCel$_{3.0}$, (b) AcCel$_{2.6}$-*b*-PDL-*b*-AcCel$_{2.6}$, and (c) AcCel$_{2.3}$-*b*-PDL-*b*-AcCel$_{2.3}$ without thermal annealing (upper) and after thermal annealing at 150 or 180 °C for 6 h (lower).

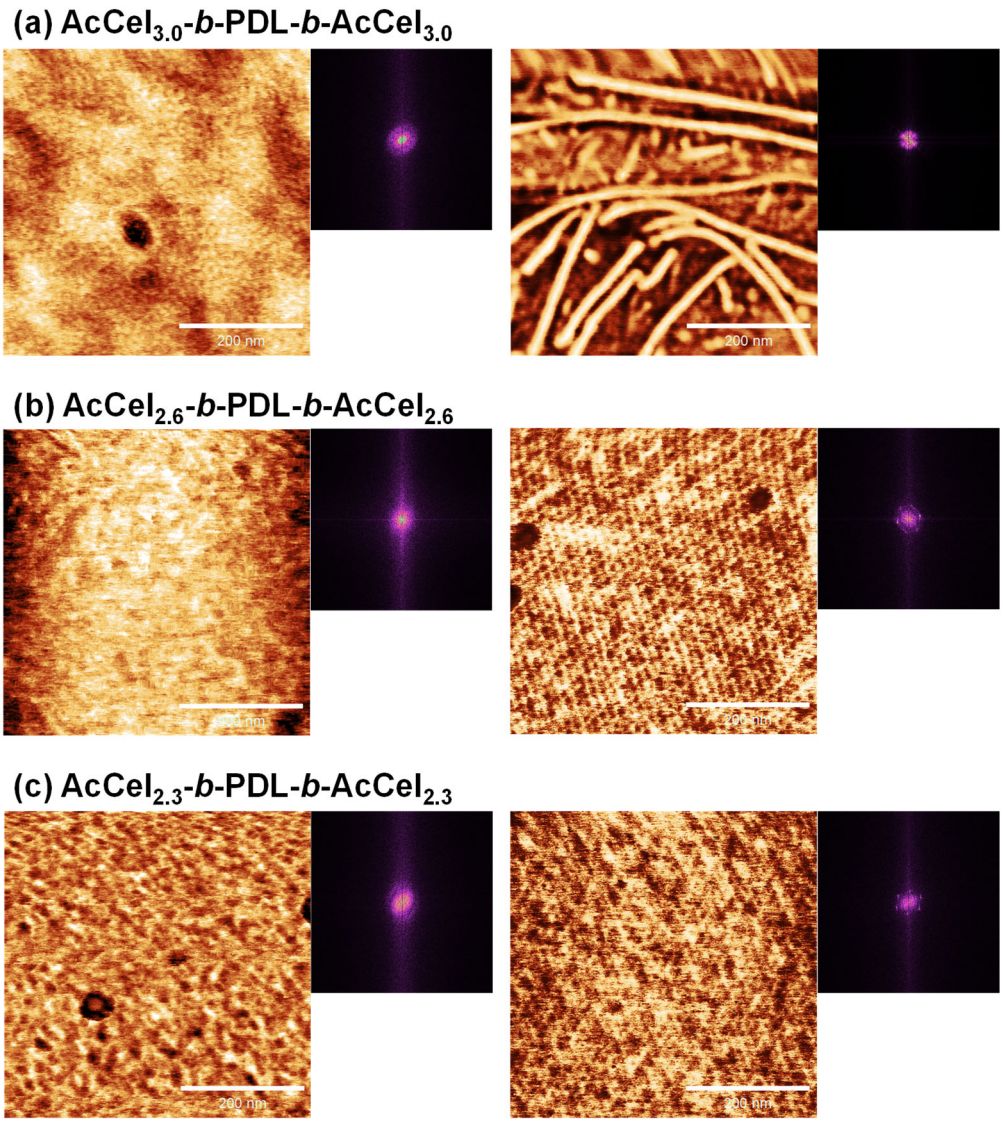


Fig. 4. AFM phase images of (a) AcCel$_{3.0}$-*b*-PDL-*b*-AcCel$_{3.0}$, (b) AcCel$_{2.6}$-*b*-PDL-*b*-AcCel$_{2.6}$, and (c) AcCel$_{2.3}$-*b*-PDL-*b*-AcCel$_{2.3}$ thin films before (left) and after (right) thermal annealing at 150 °C (AcCel$_{3.0}$-*b*-PDL-*b*-AcCel$_{3.0}$ and AcCel$_{2.6}$-*b*-PDL-*b*-AcCel$_{2.6}$) or 180 °C (AcCel$_{2.3}$-*b*-PDL-*b*-AcCel$_{2.3}$) for 6 h. The insets show the corresponding FFT profiles. Scale bars are 200 nm.

In situ SAXS measurements were performed during heating to elucidate the order–disorder temperature (T_{ODT}) (**Fig. S19**). The SAXS profiles were acquired at 10 °C steps upon heating from 30 to 280 °C. The primary scattering peak of each sample became sharper as the temperature increased to ~170 °C and then broadened at higher temperatures. Importantly, multiple scattering peaks attributed to BCC structures were observed at temperatures of 170–190 and 170–210 °C in

the SAXS profiles of AcCel$_{2.6}$-*b*-PDL-*b*-AcCel$_{2.6}$ and AcCel$_{2.3}$-*b*-PDL-*b*-AcCel$_{2.3}$, respectively. This behavior suggested that the mobility of the polymer chains increased up to a certain temperature, which induced microphase separation. Notably, the SAXS profile of AcCel$_{3.0}$-*b*-PDL-*b*-AcCel$_{3.0}$ also exhibited multiple scattering peaks attributed to BCC structures at 150–160 °C. This would be because the crystallization does not occur at these temperatures. Thus, AcCel$_{3.0}$-*b*-PDL-*b*-AcCel$_{3.0}$ has sufficient potential for microphase separation in this temperature range, where the AcCel$_{3.0}$ segment does not crystallize; nevertheless, the driving force for crystallization overwhelms that for microphase separation as the temperature decreases, resulting in the formation an ill-ordered fiber structure. Consequently, an ordered microphase-separated structure was not observed in the SAXS profile of AcCel$_{3.0}$-*b*-PDL-*b*-AcCel$_{3.0}$ at room temperature.

The full width at half maximum (FWHM) of the primary scattering peak was plotted against the measurement temperature, and the T_{ODT} was determined as the temperature at which a change in the slope was observed (**Fig. 5**). The T_{ODT} of AcCel$_{3.0}$-*b*-PDL-*b*-AcCel$_{3.0}$, AcCel$_{2.6}$-*b*-PDL-*b*-AcCel$_{2.6}$, and AcCel$_{2.3}$-*b*-PDL-*b*-AcCel$_{2.3}$ were estimated to be 181, 233, and 246 °C, respectively. Considering the comparable N and f_{PDL} values of the three BCPs, the increase in T_{ODT} as the DS of the AcCel$_x$ segment decreased indicates a corresponding increase in the χ value (Bates & Fredrickson, 1990). This hypothesis is supported by the observation that AcCel$_{2.6}$-*b*-PDL-*b*-AcCel$_{2.6}$ and AcCel$_{2.3}$-*b*-PDL-*b*-AcCel$_{2.3}$ are more likely to form microphase-separated structures than AcCel$_{3.0}$-*b*-PDL-*b*-AcCel$_{3.0}$. The increase in the χ value was attributed to the enhanced hydrophilicity of the cellulosic block, which increased the repulsion with the hydrophobic PDL block. Enhanced intrablock interactions via hydrogen bonding between the hydroxy groups on the cellulosic block could also contribute to an increase in χ with decreasing DS. Several previous studies have proposed that the χ value can be increased by enhancing intrablock interactions in typical AB-diblock BCPs (Yoshida et al., 2018; Zhou et al., 2016). Overall, the SAXS and AFM results indicate that the microphase separation behavior of cellulooligosaccharide acetate-based BCPs in both the bulk and thin film states can be controlled by adjusting the DS.

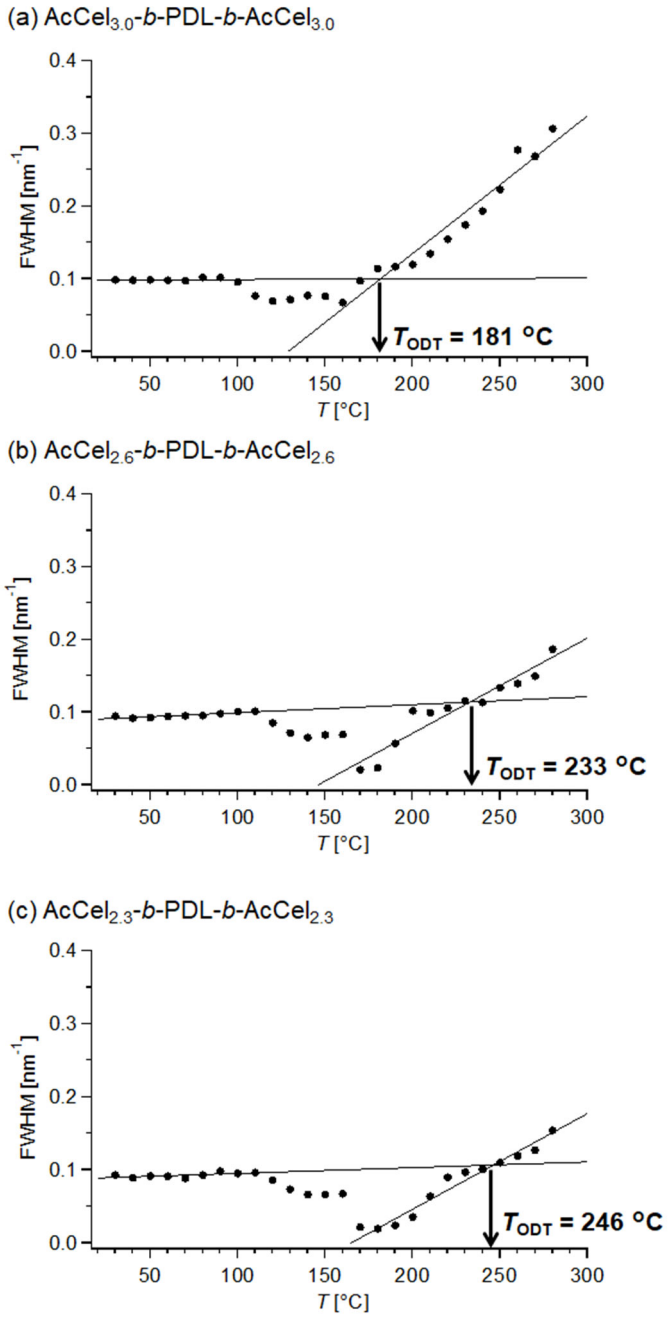


Fig. 5. Dependence of the FWHM of the primary scattering peak on the measurement temperature for (a) AcCel$_{3.0}$-*b*-PDL-*b*-AcCel$_{3.0}$, (b) AcCel$_{2.6}$-*b*-PDL-*b*-AcCel$_{2.6}$, and (c) AcCel$_{2.3}$-*b*-PDL-*b*-AcCel$_{2.3}$.

3.5. Mechanical properties

Tensile tests were conducted to evaluate the potential of AcCel$_x$-*b*-PDL-*b*-AcCel$_x$ as elastomeric materials. The film samples for the tensile tests were prepared using the same procedure as for the SAXS measurements and then cut into dog-bone shapes. The stress–strain curves are

shown in **Fig. 6** and the key mechanical properties (Young's modulus (E), strain at break (ε_b), stress at break (σ_b), and toughness) are summarized in **Table 2**. The stress–strain curves of AcCel$_x$-*b*-PDL-*b*-AcCel$_x$ did not show a yield point, regardless of the annealing history, indicating that these samples have elastomeric properties (**Fig. 6**). In addition, for tensile tests with 10 loading/unloading cycles, all the samples showed a small hysteresis loop, which further supported their sufficient elastic recovery (**Fig. S20**).

The σ_b values of non-annealed AcCel$_{2.6}$-*b*-PDL-*b*-AcCel$_{2.6}$ (2.68 ± 0.08 MPa) and AcCel$_{2.3}$-*b*-PDL-*b*-AcCel$_{2.3}$ (2.14 ± 0.01 MPa) were slightly higher than that of AcCel$_{3.0}$-*b*-PDL-*b*-AcCel$_{3.0}$ (1.94 ± 0.13 MPa). Similarly, the ε_b values of non-annealed AcCel$_{2.6}$-*b*-PDL-*b*-AcCel$_{2.6}$ (420 ± 15%) and AcCel$_{2.3}$-*b*-PDL-*b*-AcCel$_{2.3}$ (378 ± 7%) were 1.2–1.3 times larger than that of AcCel$_{3.0}$-*b*-PDL-*b*-AcCel$_{3.0}$ (320 ± 5%). The same trend was observed for the annealed samples, with the ε_b values of 192 ± 5%, 310 ± 10%, and 317 ± 10% for AcCel$_{3.0}$-*b*-PDL-*b*-AcCel$_{3.0}$, AcCel$_{2.6}$-*b*-PDL-*b*-AcCel$_{2.6}$, and AcCel$_{2.3}$-*b*-PDL-*b*-AcCel$_{2.3}$, respectively. These results indicate that reducing the DS effectively improves the mechanical properties of AcCel$_x$-*b*-PDL-*b*-AcCel$_x$.

Interestingly, the E value of annealed AcCel$_{3.0}$-*b*-PDL-*b*-AcCel$_{3.0}$ (4.93 ± 0.07 MPa) was three times larger than that of non-annealed AcCel$_{3.0}$-*b*-PDL-*b*-AcCel$_{3.0}$ (1.64 ± 0.07 MPa), whereas the E values of AcCel$_{2.6}$-*b*-PDL-*b*-AcCel$_{2.6}$ (1.5–1.6 MPa) and AcCel$_{2.3}$-*b*-PDL-*b*-AcCel$_{2.3}$ (1.2–1.4 MPa) were not significantly affected by thermal annealing. This difference could be due to the high crystallinity of the annealed AcCel$_{3.0}$ segment. Indeed, for some BCP systems, it has been reported that enhanced crystallinity increases the modulus, although ε_b decreases (Jauzein, Huneault, & Heuzey, 2017; Sarasua, Arraiza, Balderdi, & Maiza, 2005; Watts & Hillmyer, 2019). Furthermore, the fiber-like structure observed in annealed AcCel$_{3.0}$-*b*-PDL-*b*-AcCel$_{3.0}$ could also be an important factor, as such a continuous hard domain would increase the E value. We previously found that a carbohydrate-based elastomer with a hexagonal cylinder (HEX) structure had a higher modulus than an elastomer with a BCC structure (Isono, Nakahira, et al., 2020). This difference originated from the continuous hard domain in the HEX structure, which could bear deformation under stretching

(Crawford & Sita, 2015).

Table 2. Tensile properties of AcCel$_x$-*b*-PDL-*b*-AcCel$_x$

BCP	Annealing	E^a [MPa]	$\varepsilon_b{}^a$ [%]	$\sigma_b{}^a$ [MPa]	Toughness^a [MPa]
AcCel$_{3.0}$-*b*-PDL-*b*-AcCel$_{3.0}$	none	1.64 ± 0.07	320 ± 5	1.94 ± 0.13	3.68 ± 0.27
	150 °C for 6 h	4.93 ± 0.07	192 ± 5	2.63 ± 0.06	3.28 ± 0.13
AcCel$_{2.6}$-*b*-PDL-*b*-AcCel$_{2.6}$	none	1.53 ± 0.03	420 ± 15	2.68 ± 0.08	5.89 ± 0.38
	150 °C for 6 h	1.56 ± 0.10	310 ± 10	2.15 ± 0.10	3.67 ± 0.24
AcCel$_{2.3}$-*b*-PDL-*b*- AcCel$_{2.3}$	none	1.38 ± 0.06	378 ± 7	2.14 ± 0.01	4.35 ± 0.13
	180 °C for 6 h	1.23 ± 0.04	317 ± 10	1.80 ± 0.10	3.11 ± 0.28

^{a}Tensile properties are shown as average values (with standard deviations) for three specimens.

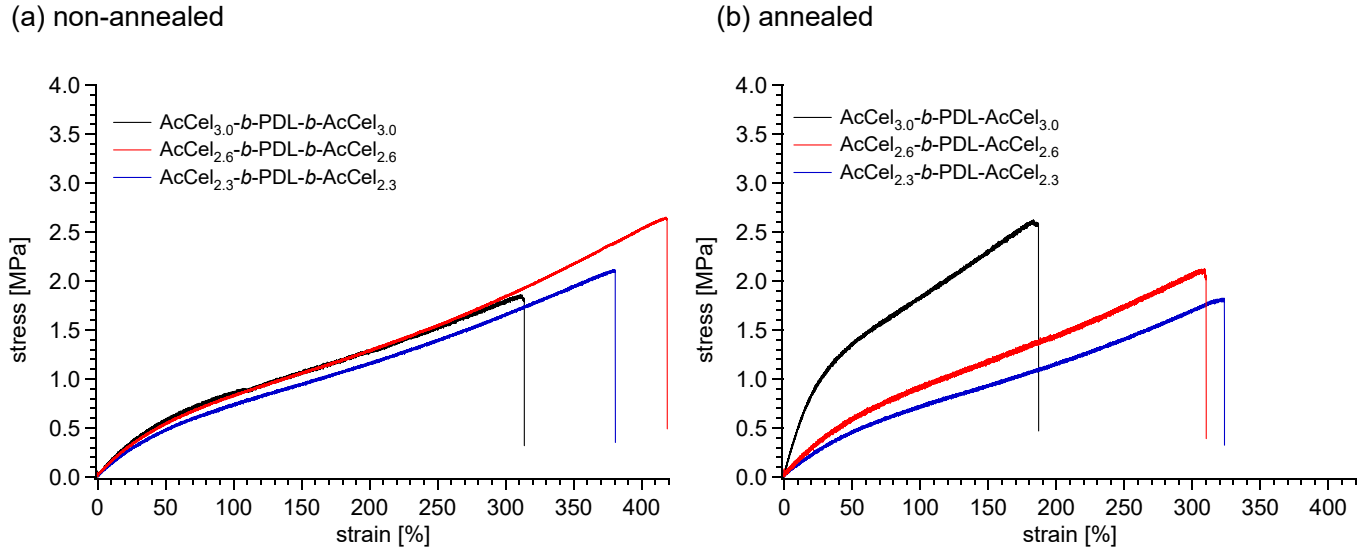


Fig. 6. Typical stress–strain curves of AcCel$_{3.0}$-*b*-PDL-*b*-AcCel$_{3.0}$ (black), AcCel$_{2.6}$-*b*-PDL-*b*-AcCel$_{2.6}$ (red), and AcCel$_{2.3}$-*b*-PDL-*b*-AcCel$_{2.3}$ (blue) (a) before and (b) after thermal annealing.

Furthermore, we investigated the stress relaxation behavior to evaluate the impact of DS on material deformation. Stress relaxation experiments were performed by monitoring the stress response of a sample under a constant applied strain of 70%. The average slope in the range of 30–300 s in the semi-log stress relaxation curve is smaller for AcCel$_{3.0}$-*b*-PDL-*b*-AcCel$_{3.0}$ (−11.5) than for AcCel$_{2.6}$-*b*-PDL-*b*-AcCel$_{2.6}$ (−9.04) and AcCel$_{2.3}$-*b*-PDL-*b*-AcCel$_{2.3}$ (−8.48), indicating that stress relaxation was suppressed as DS decreased (**Fig. 7**). The stronger intermolecular forces

derived from hydrogen bonding in the $AcCel_{2.6}$ and $AcCel_{2.3}$ segments likely prevented chain pullout and suppressed stress relaxation. Elastomers bearing hydrogen bonding motifs on their hard segments have been found to exhibit less stress relaxation than those without hydrogen bonds.(Watts & Hillmyer, 2019) This stronger hydrogen bonding also improves the mechanical properties, such as σ_b and ε_b. In addition, the higher potential of $AcCel_{2.6}$-*b*-PDL-*b*-$AcCel_{2.6}$ and $AcCel_{2.3}$-*b*-PDL-*b*-$AcCel_{2.3}$ to form ordered microphase-separated structures could decrease stress relaxation by increasing the energy required for chain pullout.(Watts & Hillmyer, 2019) Overall, the tensile and stress relaxation tests reveal that the DS is a highly important factor for controlling the mechanical properties of cellulose-based elastomers.

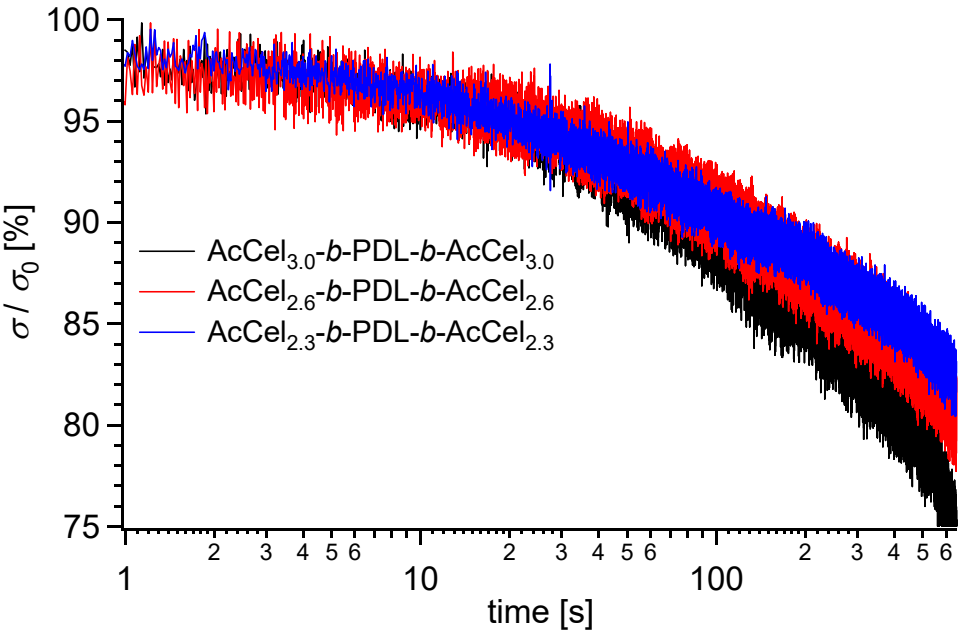


Fig. 7. Stress relaxation curves of $AcCel_{3.0}$-*b*-PDL-*b*-$AcCel_{3.0}$ (black), $AcCel_{2.6}$-*b*-PDL-*b*-$AcCel_{2.6}$ (red), and $AcCel_{2.3}$-*b*-PDL-*b*-$AcCel_{2.3}$ (blue) at 70% strain.

3.6. Biodegradability

Cellulose acetate with a lower DS is more susceptible to biodegradation; (Edgar et al., 2001; Erdal & Hakkarainen, 2022; Kliem et al., 2020; Puls et al., 2011) thus, we investigated the effect of DS on the biodegradability of $AcCel_x$-*b*-PDL-*b*-$AcCel_x$. We performed a preliminary biodegradability test with the non-annealed $AcCel_x$-*b*-PDL-*b*-$AcCel_x$ specimens in a recirculating

aquaculture system (freshwater environment) in which tilapia had lived for 8 weeks. The water temperature and number of viable bacteria samples were 26 °C and 900 CFU/mL, respectively (for details, see the SI). None of the specimens exhibited an obvious change in appearance, and NMR and SEC analyses revealed no significant changes before and after the biodegradation test (**Figs. S21**–**25**). However, scanning electron microscopy (SEM) observations revealed that microorganisms were adhered to the AcCel$_x$-*b*-PDL-*b*-AcCel$_x$ film surfaces after the biodegradation test (**Fig. 8**). Interestingly, holes with diameters of <1 μm were observed in the AcCel$_{2.6}$-*b*-PDL-*b*-AcCel$_{2.6}$ and AcCel$_{2.3}$-*b*-PDL-*b*-AcCel$_{2.3}$ films but not in the AcCel$_{3.0}$-*b*-PDL-*b*-AcCel$_{3.0}$ film. These holes, which were likely formed by a microbial degradation process, indicate that the biodegradation potential increased as the DS decreased. Considering the NMR spectra and SEC results, biodegradation was assumed to proceed only on the surface of the AcCel$_x$-*b*-PDL-*b*-AcCel$_x$ films. Nevertheless, these results demonstrate that biodegradability of AcCel$_x$-*b*-PDL-*b*-AcCel$_x$ can be improved by simply tuning the DS of the hard segment. However, further long-term tests are required to obtain a comprehensive understanding of this process, and details of the biodegradation behavior in aqueous environments are currently being investigated.

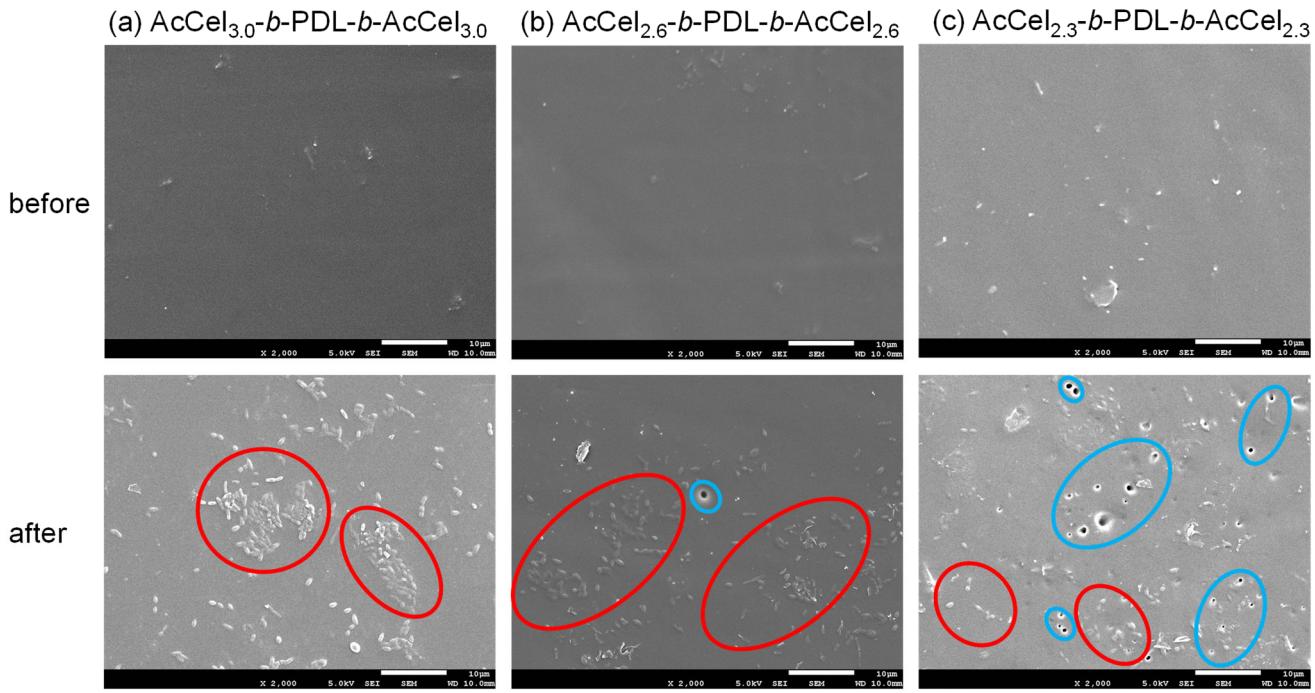


Fig. 8. SEM images of (a) AcCel$_{3.0}$-*b*-PDL-*b*-AcCel$_{3.0}$, (b) AcCel$_{2.6}$-*b*-PDL-*b*-AcCel$_{2.6}$, and (c)

692 $AcCel_{2.3}$-*b*-PDL-*b*-$AcCel_{2.3}$ films before (upper) and after (lower) degradation tests. The red and
693 blue circles show microorganism and newly formed holes, respectively. Scale bars are 10 μm.
694
695 **4. Conclusion**
696 We used a combination of CDP-mediated cellooligosaccharide synthesis, ring-opening
697 polymerization, and a click reaction to synthesize cellulose-based BCPs, $AcCel_x$-*b*-PDL-*b*-$AcCel_x$,
698 consisting of cellooligosaccharide acetate ($AcCel_x$) hard segments with three different DSs and only
699 one molecular weight PDL soft segments. The microphase separation behavior and mechanical
700 properties of $AcCel_x$-*b*-PDL-*b*-$AcCel_x$ were found to be highly dependent on the DS of the $AcCel_x$
701 segment. In particular, the stronger intermolecular interactions (i.e., hydrogen bonding) associated
702 with decreasing DS positively affected these properties. The findings of this study clearly
703 demonstrate that DS is a useful factor for improving and optimizing the physical properties of
704 cellulose acetate-based TPEs. In addition, we found that the biodegradability of $AcCel_x$-*b*-PDL-*b*-
705 $AcCel_x$ in an aqueous environment increased as the DS decreased. Although further detailed
706 biodegradation studies are necessary, this tendency is consistent with the fact that cellulose acetate
707 itself is more susceptible to biodegradation when the DS is low (Edgar et al., 2001; Erdal &
708 Hakkarainen, 2022; Kliem et al., 2020; Puls et al., 2011). Overall, DS was found to influence a
709 range of material properties for not only cellulose acetate but also cellulose acetate-based BCPs.
710 This approach can be expanded to the molecular design of a wide range of poly- or oligosaccharide-
711 based BCP materials and will contribute to the development of next-generation environmentally
712 benign polymeric materials that can replace conventional petroleum-based materials.
713
714 **Funding**
715 This work was supported by JSPS Grants-in-Aid for Scientific Research (B) (Nos.
716 19H02549, 20H02792, and 19H02769), the JSPS Fund for the Promotion of Joint International
717 Research (B) (No. 21KK0096), the Japan Science and Technology Agency (JST) COI-NEXT

program (Grant Number JPMJPF2102), “Bio-organic Material Recycle System in Space” on MEXT Coordination Funds for Promoting AeroSpace Utilization (Grant Number JPJ000959), the Frontier Chemistry Center (Hokkaido University), the Photoexcitonix Project (Hokkaido University), the Creative Research Institute (Hokkaido University), the Project of Junior Scientist Promotion in Hokkaido University, the Iketani Science and Technology Foundation, the Asahi Glass Foundation, and Toyota Riken.

Acknowledgement

This work was, in part, conducted under the approval of the Photon Factory Program Advisory Committee (Proposal nos. 2019G579 and 2021G531). The authors thank Prof. Motomitsu Kitaoka (Niigata University) for providing the pET28a-CDP plasmid, Prof. Hajime Ito (Hokkaido University) for assistance with AFM observations, Mr. Kenji Ohkubo (Hokkaido University) and Mr. Tetsuya Konishi (Hokkaido University) for assistance with SEM observations, and Mr. Hiroyuki Itaya (Kanazawa University) and Ms. Kaoru Kitani (Kanazawa University) for assistance with biodegradation tests.

References

Bates, F. S., & Fredrickson, G. H. (1990). Block Copolymer Thermodynamics: Theory and Experiment. *Annual Review of Physical Chemistry*, *41*, 525–557.

Cerqueira, D. A., Valente, A. J. M., Filho, G. R., & Burrows, H. D. (2009). Synthesis and properties of polyaniline-cellulose acetate blends: The use of sugarcane bagasse waste and the effect of the substitution degree. *Carbohydrate Polymers*, *78*, 402–408.

Crawford, K. E., & Sita, L. R. (2015). *De Novo* Design of a New Class of “Hard-Soft” Amorphous, Microphase-Separated, Polyolefin Block Copolymer Thermoplastic Elastomers. *ACS Macro Letters*, *4*, 921–925.

de Freitas, R. R. M., Senna, A. M., & Botaro, V. R. (2017). Influence of degree of substitution on

744 thermal dynamic mechanical and physicochemical properties of cellulose acetate. *Industrial*
745 *Crops and Products*, *109*, 452–458.
746 Edgar, K. J., Buchanan, C. M., Debenham, J. S., Rundquist, P. A., Seiler, B. D., Shelton, M. C., &
747 Tindall, D. (2001). Advances in cellulose ester performance and applicaton. *Progress Polymer*
748 *Science*, *26*, 1605–1688.
749 Erdal, N. B., & Hakkarainen, M. (2022). Degradation of Cellulose Derivatives in Laboratory , Man-
750 Made, and Natural Environments. *Biomacromolecules*, *23*, 2713–2729.
751 Fournier, L., Rivera Mirabal, D. M., & Hillmyer, M. A. (2022). Toward Sustainable Elastomers
752 from the Grafting-Through Polymerization of Lactone-Containing Polyester Macromonomers.
753 *Macromolecules*, *55*, 1003–1014.
754 Grandjean, C., Boutonnier, A., Guerreiro, C., Fournier, J.-M., & Mulard, L. A. (2005). On the
755 Preparation of Carbohydrate-Protein Conjugates Using the Traceless Staudinger Ligation. The
756 Journal of Organic Chemistry, 70, 7123–7132.
757 Halila, S., Manguian, M., Fort, S., Cottaz, S., Hamaide, T., Fleury, E., & Driguez, H. (2008).
758 Synthesis of Well-Defined Glyco-Polyorganosiloxanes by “Click” Chemistry and their
759 Surfactant Properties. Macromolecular Chemistry and Physics, 209, 1282–1290.
760 Hata, Y., & Serizawa, T. (2021). Self-assembly of cellulose for creating green materials with tailor-
761 made nanostructures. *Journal of Materials Chemistry B*, *9*, 3944–3966.
762 He, W.-N., & Xu, J.-T. (2012). Crystallizaiton assisited self-assembly of semicrystalline block
763 copolymers. *Progress in Polymer Science*, *37*, 1350–1400.
764 Hiraishi, M., Igarashi, K., Kimura, S., Wada, M., Kitaoka, M., & Samejima, M. (2009). Synthesis
765 of highly ordered cellulose II in vitro using cellodextrin phosphorylase. *Carbohydrate*
766 *Research*, *344*, 2468–2473.
767 Isono, T., Kawakami, N., Watanabe, K., Yoshida, K., Otsuka, I., Mamiya, H., Ito, H., Yamamoto,
768 T., Tajima, K., Borsali, R., & Satoh, T. (2019). Microphase separation of carbohydrate-based
769 star-block copolymers with sub-10 nm periodicity. *Polymer Chemistry*, *10*, 1119–1129.

770 Isono, T., Komaki, R., Kawakami, N., Chen, K., Chen, H.-L., Lee, C., Suzuki, K., Ree, B. J.,
771 Mamiya, H., Yamamoto, T., Borsali, R., Tajima, K., & Satoh, T. (2022). Tailored Solid-State
772 Carbohydrate Nanostructures Based on Star-Shaped Discrete Block Co-Oligomers.
773 *Biomacromolecules*. *23*, 3978–3989.
774 Isono, T., Komaki, R., Lee, C., Kawakami, N., Ree, B. J., Watanabe, K., Yoshida, K., Mamiya, H.,
775 Yamamoto, T., Borsali, R., Tajima, K., & Satoh, T. (2020). Rapid access to discrete and
776 monodisperse block co-oligomers from sugar and terpenoid toward ultrasmall periodic
777 nanostructures. *Communications Chemistry*, *3*, 1–9.
778 Isono, T., Nakahira, S., Hsieh, H. C., Katsuhara, S., Mamiya, H., Yamamoto, T., Chen, W. C.,
779 Borsali, R., Tajima, K., & Satoh, T. (2020). Carbohydrates as Hard Segments for Sustainable
780 Elastomers: Carbohydrates Direct the Self-Assembly and Mechanical Properties of Fully Bio-
781 Based Block Copolymers. *Macromolecules*, *53*, 5408–5417.
782 Isono, T., Otsuka, I., Kondo, Y., Halila, S., Fort, S., Rochas, C., Satoh, T., Borsali, R., & Kakuchi,
783 T. (2013). Sub-10 nm Nano-Organization in AB_2- and AB_3-Type Miktoarm Star Copolymers
784 Consisting of Maltoheptaose and Polycaprolactone. *Macromolecules*, *46*, 1461–1469.
785 Isono, T., Ree, B. J., Tajima, K., Borsali, R., & Satoh, T. (2018). Highly Ordered Cylinder
786 Morphologies with 10 nm Scale Periodicity in Biomass-Based Block Copolymers.
787 *Macromolecules*, *51*, 428–437.
788 Jauzein, T., Huneault, M. A., & Heuzey, M.-C. (2017). Crystallinity and mechanical properties of
789 polylactide/ether-amide copolymer blends. *Journal of Applied Polymer Science*, *134*, 1–10.
790 Kamide, K., & Saito, M. (1985) Thermal Analysis of Cellulose Acetate Solids with Toal Degrees of
791 Substitution of 0.49, 1.75, 2.46, and 2.92. *Polymer Journal*, *17*, 919–928.
792 Kamitakahara, H., Enomoto, Y., Hasegawa, C., & Nakatsubo, F. (2005). Synthesis of Diblock
793 Copolymers With Cellulose Derivatives. 2. Characterization and Thermal Properties of
794 Cellulose Triacetate-Block-Oligoamide-15. *Cellulose*, *12*, 527–541.
795 Katsuhara, S., Mamiya, H., Yamamoto, T., Tajima, K., Isono, T., & Satoh, T. (2020).

Metallopolymer-*block*-oligosaccharide for sub-10 nm microphase separation. *Polymer Chemistry*, *11*, 2995–3002.

Katsuhara, S., Takagi, Y., Sunagawa, N., Igarashi, K., Yamamoto, T., Tajima, K., Isono, T., & Satoh, T. (2021). Enhanced Self-Assembly and Mechanical Properties of Cellulose-Based Triblock Copolymers: Comparisons with Amylose-Based Triblock Copolymers. *ACS Sustainable Chemistry and Engineering*, *9*, 9779–9788.

Kliem, S., Kreutzbruck, M., & Bonten, C. (2020) Reviwe on the Biological Degradation of Polymer in Various Environments. *Materilas*, *13*, 4586

Kono, H., Hashimoto, H., & Shimizu, Y. (2015). NMR characterization of cellulose acetate: Chemical shift assignments, substituent effects, and chemical shift additivity. *Carbohydrate Polymers*, *118*, 91–100.

Kuga, T., Sunagawa, N., & Igarashi, K. (2022). Enzymatic synthesis of cellulose in space: gravity is a crucial factor for building cellulose II gel structure. *Cellulose*, *29*, 2999–3015.

Liffland, S., & Hillmyer, M. A. (2021). Enhanced Mechanical Properties of Aliphatic Polyester Thermoplastic Elastomers through Star Block Architectures. *Macromolecules*, *54*, 9327–9340.

Maji, P., & Naskar, K. (2022). Styrenic block copolymer-based thermoplastic elastomers in smart applications: Advances in synthesis, microstructure, and structure–property relationships—A review. *Journal of Applied Polymer Science*, *139*, e52942.

Martello, M. T., Schneiderman, D. K., & Hillmyer, M. A. (2014). Synthesis and Melt Processing of Sustainable Poly(ε-decalactone)-*block*-poly(lactide) Multiblock Thermoplastic Elastomers. *ACS Sustainable Chemistry and Engineering*, *2*, 2519–2526.

Mumtaz, M., Takagi, Y., Mamiya, H., Tajima, K., Bouilhac, C., Isono, T., Satoh, T., & Borsali, R. (2020). Sweet Pluronic poly(propylene oxide)-*b*-oligosaccharide block copolymer systems: Toward sub-4 nm thin-film nanopattern resolution. *European Polymer Journal*, *134*, 109831.

Nishimura, T., Katsuhara, S., Lee, C., Ree, B. J., Borsali, R., Yamamoto, T., Tajima, K., Satoh, T., & Isono, T. (2022). Fabrication of Ultrafine, Highly Ordered Nanostructures Using

822 Carbohydrate-Inorganic Hybrid Block Copolymers. *Nanomaterials*, *12*, 1–14.
823 Petrović, D. M., Kok, I., Woortman, A. J. J., Ćirić, J., & Loos, K. (2015). Characterization of
824 Oligocellulose Synthesized by Reverse Phosphorolysis Using Different Cellodextrin
825 Phosphorylases. *Analytical Chemistry*, *87*, 9639–9646.
826 Puls, J., Wilson, S. A., & Hölter, D. (2011). Degradation of Cellulose Acetate-Based Materials: A
827 Review. *Journal of Polymers and the Environment*, *19*, 152–165.
828 Pylkkänen, R., Mohammadi, P., Arola, S., De Ruijter, J. C., Sunagawa, N., Igarashi, K., & Penttilä,
829 M. (2020). In Vitro Synthesis and Self-Assembly of Cellulose II Nanofibrils Catalyzed by the
830 Reverse Reaction of *Clostridium thermocellum* Cellodextrin Phosphorylase.
831 *Biomacromolecules*, *21*, 4355–4364.
832 Sarasua, J. R., Arraiza, A. L., Balerdi, P., & Maiza, I. (2005). Crystallinity and Mechanical
833 Properties of Optically Pure Polylactides and Their Blends. *Polymer Engineering and Science*,
834 *45*, 745–753.
835 Serizawa, T., Kato, M., Okura, H., Sawada, T., & Wada, M. (2016). Hydrolytic activities of
836 artificial nanocellulose synthesized via phosphorylase-catalyzed enzymatic reactions. *Polymer*
837 *Journal*, *48*, 539–544.
838 Shin, J., Martello, M. T., Shrestha, M., Wissinger, J. E., Tolman, W. B., & Hillmyer, M. A. (2011).
839 Pressure-Sensitive Adhesives from Renewable Triblock Copolymers. *Macromolecules*, *44*,
840 87–94.
841 Sugiura, K., Saito, M., Sawada, T., Tanaka, H., & Serizawa, T. (2022). Cellodextrin Phosphorylase-
842 Catalyzed Single-Process Production and Superior Mechanical Properties of Organic −
843 Inorganic Hybrid Hydrogels Composed of Surface-Carboxylated Synthetic Nanocelluloses and
844 Hydroxyapatite. *ACS Sustainable Chemistry and Engineering*, *10*, 13484–13494.
845 Sugiura, K., Sawada, T., Tanaka, H., & Serizawa, T. (2021). Enzyme-catalyzed propagation of
846 cello-oligosaccharide chains from bifunctional oligomeric primers for the preparation of block
847 co-oligomers and their crystalline assemblies. *Polymer Journal*, *53*, 1133–1143.

Tezuka, Y., & Tsuchiya, Y. (1995). Determination of substituent distribution in cellulose acetate by means of a ^{13}C NMR study on its propanoated derivative. *Carbohydrate Research*, *273*, 83–91.

Watts, A., & Hillmyer, M. A. (2019). Aliphatic Polyester Thermoplastic Elastomers Containing Hydrogen-Bonding Ureidopyrimidinone Endgroups. *Biomacromolecules*, *20*, 2598–2609.

Watts, A., Kurokawa, N., & Hillmyer, M. A. (2017). Strong, Resilient, and Sustainable Aliphatic Polyester Thermoplastic Elastomers. *Biomacromolecules*, *18*, 1845–1854.

Yoshida, K., Tian, L., Miyagi, K., Yamazaki, A., Mamiya, H., Yamamoto, T., Tajima, K., Isono, T., & Satoh, T. (2018). Facile and Efficient Modification of Polystyrene-*block*-poly(methyl methacrylate) for Achieving Sub-10 nm Feature Size. *Macromolecules*, *51*, 8064–8072.

Zhou, S. X., Janes, D. W., Kim, C. Bin, Willson, C. G., & Ellison, C. J. (2016). Designing Intrablock Attractions to Increase the χ Parameter of a Symmetric Diblock Copolymer. *Macromolecules*, *49*, 8332–8340.